



HAL
open science

Syn-orogenic fluid flow in the Jaca basin (south Pyrenean fold and thrust belt) from fracture and vein analyses

Nemo Crognier, Guilhem Hoareau, Charles Aubourg, Michel Dubois, Brice Lacroix, Matthieu Branellec, Jean-Paul Callot, Torsten Vennemann

► **To cite this version:**

Nemo Crognier, Guilhem Hoareau, Charles Aubourg, Michel Dubois, Brice Lacroix, et al.. Syn-orogenic fluid flow in the Jaca basin (south Pyrenean fold and thrust belt) from fracture and vein analyses. *Basin Research*, 2018, 30 (2), pp.187-216. 10.1111/bre.12249 . hal-01804359

HAL Id: hal-01804359


<https://hal.science/hal-01804359>

Submitted on 20 Jun 2024

HAL is a multi-disciplinary open access archive for the deposit and dissemination of scientific research documents, whether they are published or not. The documents may come from teaching and research institutions in France or abroad, or from public or private research centers.

L'archive ouverte pluridisciplinaire **HAL**, est destinée au dépôt et à la diffusion de documents scientifiques de niveau recherche, publiés ou non, émanant des établissements d'enseignement et de recherche français ou étrangers, des laboratoires publics ou privés.

Syn-orogenic fluid flow in the Jaca basin (south Pyrenean fold and thrust belt) from fracture and vein analyses

N. Crognier,* G. Hoareau,*  C. Aubourg,* M. Dubois,† B. Lacroix,‡ M. Branellec,* J. P. Callot* and T. Vennemann§

*CNRS/TOTAL/UNIV PAU & PAYS ADOUR, Laboratoire des Fluides Complexes et leurs Réservoirs-IPRA, UMR5150, Pau, France

†Laboratoire de Génie Civil et de géo-Environnement (LGCgE, EA 4515), Université Lille 1, Villeneuve d'Ascq, France

‡Department of Geology, Kansas State University, Manhattan, KS, USA

§Faculté des Géosciences et de l'environnement, Institut des dynamiques de la Surface Terrestre (IDYST), Quartier UNIL-Mouline Bâtiment Géopolis 4634, Lausanne, Switzerland

ABSTRACT

This study aims at understanding the origin and nature of syn-orogenic fluid flow in the Jaca basin from the South Pyrenean fold and thrust-belt, as recorded in calcite and quartz veins of the Sierras Interiores (Spain) and the turbiditic basin, which cover upper Cretaceous to Late Eocene syntectonic deposits. The fracture network consists of a classical pattern of transverse and longitudinal fractures related to Layer Parallel Shortening (LPS) and folding respectively. Veins filled equally about the third of fractures in the carbonate shelf and turbidites. Carbon and oxygen isotopes of calcite veins mostly indicate precipitation from isotopically buffered water, consistent with high water-rock interaction. In the Sierras Interiores, petrographical observations and fluid inclusion microthermometry are consistent with two distinct stages of precipitation. The first stage is characterized by relatively low Th and low salinities (155–205 °C and 0.5–3.2 wt% eq. NaCl). The second stage, which was characterized both by the formation of mode-I joints and by mode-I reactivation of pre-existing veins, shows higher Th and salinities (215–270 °C and 2.2–5.7 wt% eq. NaCl). Waters recorded in the second stage are interpreted to have interacted with underlying Triassic evaporites and flowed along major thrusts before vein precipitation, which are locally in thermal disequilibrium with host-rocks. We suggest the transition from a rather closed hydrological system during the first stage of vein formation, interpreted to have occurred during Eaux-chaudes thrusting (upper Lutetian–Bartonian), to a more open hydrological system during the second stage, which likely occurred during Gavarnie thrusting (Priabonian–early Rupelian). Finally, we also document the migration in space and time of hydrothermal pulses along the South Pyrenean Foreland Basin, related to the westward propagation of major thrusts during the Pyrenean orogeny.

INTRODUCTION

Fold and thrust belts represent 14% of the world's discovered reserves of hydrocarbons (Cooper, 2007). In such compressive context, the evolution of hydrocarbon reservoir properties depends on the fluid flow behaviour and pathways (Macgregor, 1996), which is in turn controlled by thrusting, fracturing, topography and lithospheric

flexure (e.g. Roure *et al.*, 2005; Evans & Fischer, 2012; Tavani *et al.*, 2015). At the fold scale, the dynamics of fluid migration becomes increasingly well understood owing to the study of the vertical persistence and the lateral connectivity of joints and veins (e.g. Fischer *et al.*, 2009; Beaudoin *et al.*, 2011, 2015; Barbier *et al.*, 2012b). However, at the scale of foreland basins, the characteristics of fluid migration during deformation are less documented (Machel *et al.*, 2000; Travé *et al.*, 2000; Evans & Fischer, 2012; Beaudoin *et al.*, 2014a,b). Most large-scale paleohydrological models derive from studies focused on single thrusts or folds, or on reduced areas (e.g. Qing & Mountjoy, 1992; Al-Aasm *et al.*, 2002; Douglas *et al.*,

Correspondence: N. Crognier, CNRS/TOTAL/UNIV PAU & PAYS ADOUR, Laboratoire des Fluides Complexes et leurs Réservoirs-IPRA, UMR5150, Pau, France.
E-mails: nemo.crognier@univ-pau.fr; nemo.crognier@gmail.com

2003; Barbier *et al.*, 2012b). Studies at the scale of entire fold and thrust belts are still needed to document the behaviour of fluid flow in both space and time, along with propagation of deformation.

The South-Pyrenean fold and thrust belt (SPFTB) (Fig. 1) is well known for numerous well exposed structures which have made it a referential for analyses of thrust activation, fracturing, fluid-rock interaction and fluid migration (Labaume *et al.*, 1985, 2016; Bradbury & Woodwell, 1987; Rye & Bradbury, 1988; Teixell, 1996; Travé *et al.*, 1997, 1998, 2000; McCaig *et al.*, 2000; Jolivet *et al.*, 2007; Mansurbeg *et al.*, 2009; Lacroix *et al.*, 2011, 2012, 2014; Beaudoin *et al.*, 2015; Hoareau *et al.*, 2015). Therefore, it is an ideal candidate to establish a consistent large-scale paleohydrological model. The recent review of Lacroix *et al.* (2014) highlighted that the fluid systems of the northern part of the SPFTB (i.e. Axial Zone of the Pyrenees) and the Jaca thrust-sheet top basin are distinct. In the Axial Zone, Rye & Bradbury (1988) and McCaig *et al.* (2000) documented the migration of hot (>250 °C) basement-involved metamorphic fluids along several thrust units. In the northern part of the Jaca basin (Sierras Interiores), Lacroix *et al.* (2011, 2012) emphasized the predominance of a closed fluid system during thrusting, showing the impact of the structural behaviour on fluid migration. In its central part (turbiditic basin), Lacroix *et al.* (2014) have pointed out the downward migration of low-temperature meteoric water along thrusts. In the southern part of the SPFTB (Sierras Exteriores), the study of the Pico del Aguila fold demonstrated that fluids were mostly stratigraphically controlled, with some circulation of formation water in fractures induced by local bending, and infiltration of meteoric water in the shallower levels (Beaudoin *et al.*, 2015).

Whereas all above-mentioned studies were based on the study of individual thrust faults or thrust-related folds, our contribution aims to constrain the links between fracture development and fluid migration at the scale of the Jaca basin. Extensive measurements of fracture and vein orientations allow to detail the history of fracturing and its link with major tectonic structures in the Sierras Interiores and turbiditic infilling of the Jaca basin. Petrographical, geochemical and fluid inclusion analyses of calcite and calcite/quartz veins are used to decipher the nature and origin of fluids, their link with surrounding sedimentary rocks, and finally to propose a palaeohydrological model for the central and northern part of the Jaca basin.

GEOLOGICAL SETTING

The Pyrenean range formed during the convergence between the Iberian and European plates, from the late Cretaceous to the early Miocene (e.g. Labaume *et al.*,

1985; Choukroune & Garrido, 1989; Roure *et al.*, 1989; Beaumont *et al.*, 2000). This doubly-vergent and asymmetric orogenic wedge is mostly structured by south-vergent thrusts, affecting both Paleozoic basement and Mesozoic-Cenozoic cover sedimentary units (e.g. Labaume *et al.*, 1985; Choukroune & Garrido, 1989; Roure *et al.*, 1989; Teixell, 1996, 1998; Beaumont *et al.*, 2000; Vergés *et al.*, 2002; Jolivet *et al.*, 2007; Teixell *et al.*, 2016). The North Pyrenean Zone corresponds to a Mesozoic hyper-extended rift basin, inverted during Pyrenean compression that started after 83 Ma (Jammes *et al.*, 2009; Lagabrielle *et al.*, 2010; Vacherat *et al.*, 2014; Teixell *et al.*, 2016). The Axial Zone corresponds to deformed Paleozoic rocks, locally covered by lower Triassic sediments (Saura & Teixell, 2006; Cantarelli *et al.*, 2013). The broad shape of the Axial Zone is an antiformal stack, affected by major top-to-south basement thrusts (e.g. Choukroune & Garrido, 1989; Roure *et al.*, 1989; Mouthereau *et al.*, 2014; Teixell *et al.*, 2016). These thrusts pass southward to a detachment in the Triassic evaporites, inducing the formation of the fold and thrust system of the South Pyrenean Zone (SPZ) (Labaume *et al.*, 1985, 2016; Teixell, 1996; Teixell *et al.*, 2016). The SPZ overthrusts the Ebro foreland basin along the South Pyrenean Frontal Thrust (Vergés & Munoz, 1990; Millán Garrido *et al.*, 1994, 1995; Garrido *et al.*, 2000) (Fig. 1).

In the SPZ, the development and clockwise rotation of thrust-ramp anticlines during the Eocene and the Oligocene (Muñoz *et al.*, 2013) led to the separation of several sub-basins. These basins are from the east to the west: the Ripoll basin, the Tremp-Graus basin, the Ainsa basin and the Jaca basin. The present study focuses on the Jaca turbiditic basin, which extends from the Boltaña and Anisclo anticlines to the east, to the Pamplona basin to the west (Figs 1 and 2). On top of the Triassic evaporites, the stratigraphy of the Jaca basin consists of a *ca.* 500 meter-thick of pre-compressional platform carbonates (Cenomanian to Santonian), followed the 100–300 m-thick synorogenic Marboré sandstone (Campanian to Maastrichtian) passing southward to continental deposits (Garumnian facies) (Figs 2 and 3). This succession is overlaid by 4.5 kilometres of siliciclastic turbidites of the Hecho Group (Ypresian to Bartonian), passing southward to proximal shelf facies (Lutetian Guara limestone) (Labaume *et al.*, 1985; Mutti *et al.*, 1988; Teixell *et al.*, 1992; Teixell, 1996; Vergés *et al.*, 2002) (Figs 2 and 3). According to Mansurbeg *et al.* (2009), the Hecho group can be divided into five tectonostratigraphic units (TSU), separated by major unconformities. During upper Ypresian to early Lutetian, TSU 1, 2 and 3 (lower Hecho turbidites) are composed of siliciclastic arenites (sandy deposits) and hybrid arenites and calcilithites (muddy sediments) which have been transported from the south-eastern deltaic system. During the Lutetian, TSU 4 and 5 (upper Hecho turbidites) are made of hybrid arenites and

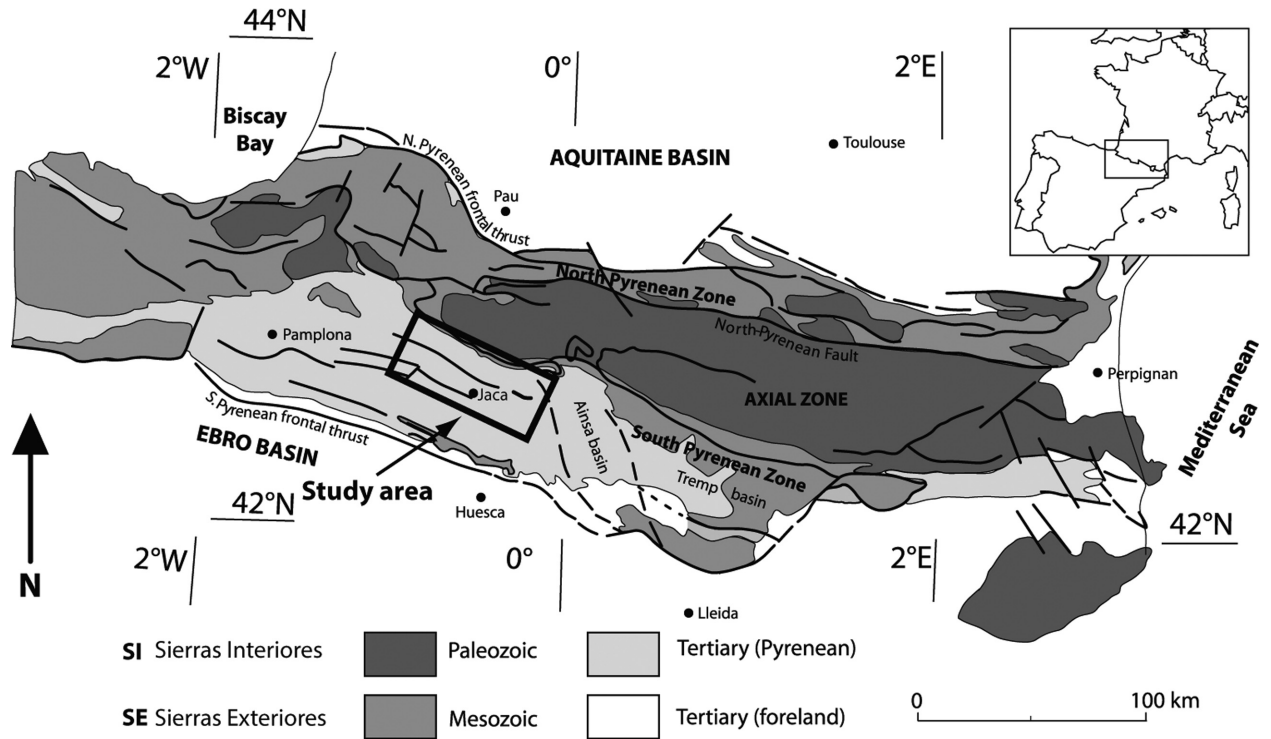


Fig. 1. Structural map of the Pyrenees with the location of the study area. Modified from Lacroix *et al.* (2011).

calclithites, with a supply direction gradually changing from the east to the north (Mansurbeg *et al.*, 2009). Nine megaturbidites (MT1 to MT9) derived from shelf carbonates were deposited in the turbiditic foredeep between the Ypresian and the Lutetian, and serve as time lines for basin-scale correlations (Labaume *et al.*, 1985). Turbiditic deposits were covered by deltaic (Larrès and Arguis-Pamplona Formations) and kilometer-thick continental units (Campodarbe and Uncastillo groups) from the Priabonian to the Aquitanian (e.g. Montes & Barnolas, 1992; Remacha & Fernández, 2003) (Figs 2 and 3).

The Jaca basin was affected by a set of imbricated south-vergent thrusts, associated with E-W striking folds (Fig. 2) (Labaume *et al.*, 1985, 2016; Teixell, 1996, 1998; Teixell *et al.*, 2016). From the mid-late Lutetian to the Bartonian, the Larra-Monte Perdido thrust system, which is rooted in the Lakora-Eaux chaudes basement thrust system, affected the Upper Cretaceous limestones and the lower part of the Hecho turbidites (Teixell, 1996) (Fig. 2). During the Priabonian-lower Rupelian, it was followed by development of the Oturia and Jaca cover thrusts, which transported the turbidites of the Hecho group over the Larrès and Arguis-Pamplona deltaic deposits. Both cover thrusts were connected to emplacement of the underlying Gavarnie basement thrust unit (Labaume *et al.*, 2016). They were responsible for the formation of Yebra de Basa and Atarès fault-propagation folds (e.g. Mutti *et al.*, 1988; Millán Garrido *et al.*, 2006), along with the southward migration of the depocentre

into the Guarga syncline, filled by *ca.* 4 km of deltaic sediments (Campodarbe group) (Labaume *et al.*, 1985; Teixell, 1996; Teixell *et al.*, 2016). Coevally to the Gavarnie emplacement, a dominant axial planar cleavage affected the lower stratigraphic sequence of the turbiditic basin. This stage probably took place during the maximum burial (Priabonian to Rupelian times), at temperature ranging between 180–215 °C (Izquierdo-Llavall *et al.*, 2013). From the mid Rupelian to the latest Oligocene-earliest Miocene the emplacement of the South-Pyrenean Thrust Front, along the Sierras Exteriores, was associated with the activity of the Guarga-Fiscal basement thrust (Fig. 2) (Labaume *et al.*, 2016). This later thrust was synchronous with deposition of continental clastic deposits of the Uncastillo formation in the southern part of the Jaca basin and in the Ebro basin (Labaume *et al.*, 1985; Teixell, 1996; Millán Garrido *et al.*, 2006; Teixell *et al.*, 2016).

METHODS

Fracture network characterization and analysis

To characterize the fracture network at the basin scale, and to highlight the impact of regional tectonics on mesoscale deformation, we analysed 3274 fractures at 48 sites located along five north-south transects and one east-west transect (Table S1 with detail sites location is provided in the auxiliary material). Fractures are grouped

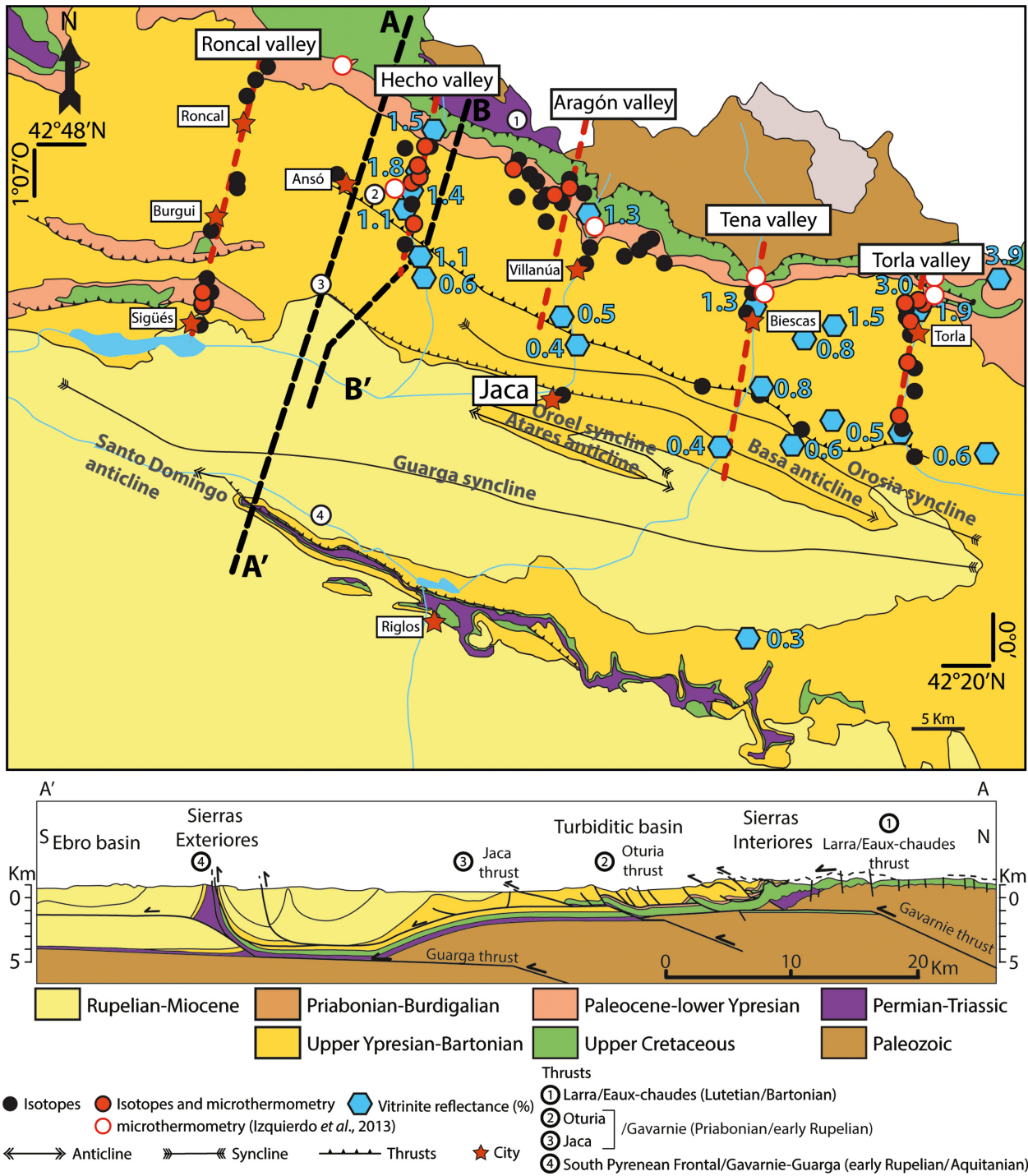


Fig. 2. Simplified geological map of the Jaca basin and cross-section along the Ansó valley redrawn from Teixell (1996). Map redrawn from available IGME 200000 maps of IGME. Vitrinite reflectances from Izquierdo-Llavall *et al.* (2013) and Labaume *et al.* (2016).

in sets based (i) on their orientation, (ii) on their dip with respect to bedding, (iii) on their chronological timing of emplacement as determined by their abutting and cross-cutting relationships, and (iv) by the presence of mineralization, or slicken fibres (e.g. Branellec *et al.*, 2015). The type of opening mode of fractures, mode I vs. mode I

+ II, is determined thanks to field observation and thin-section analysis. Contoured density diagrams at 1% area on fracture poles are calculated using Stereonet© software (Cardozo & Allmendinger, 2013). Outlier data, away from the data concentration are not considered in our analysis. We attributed each

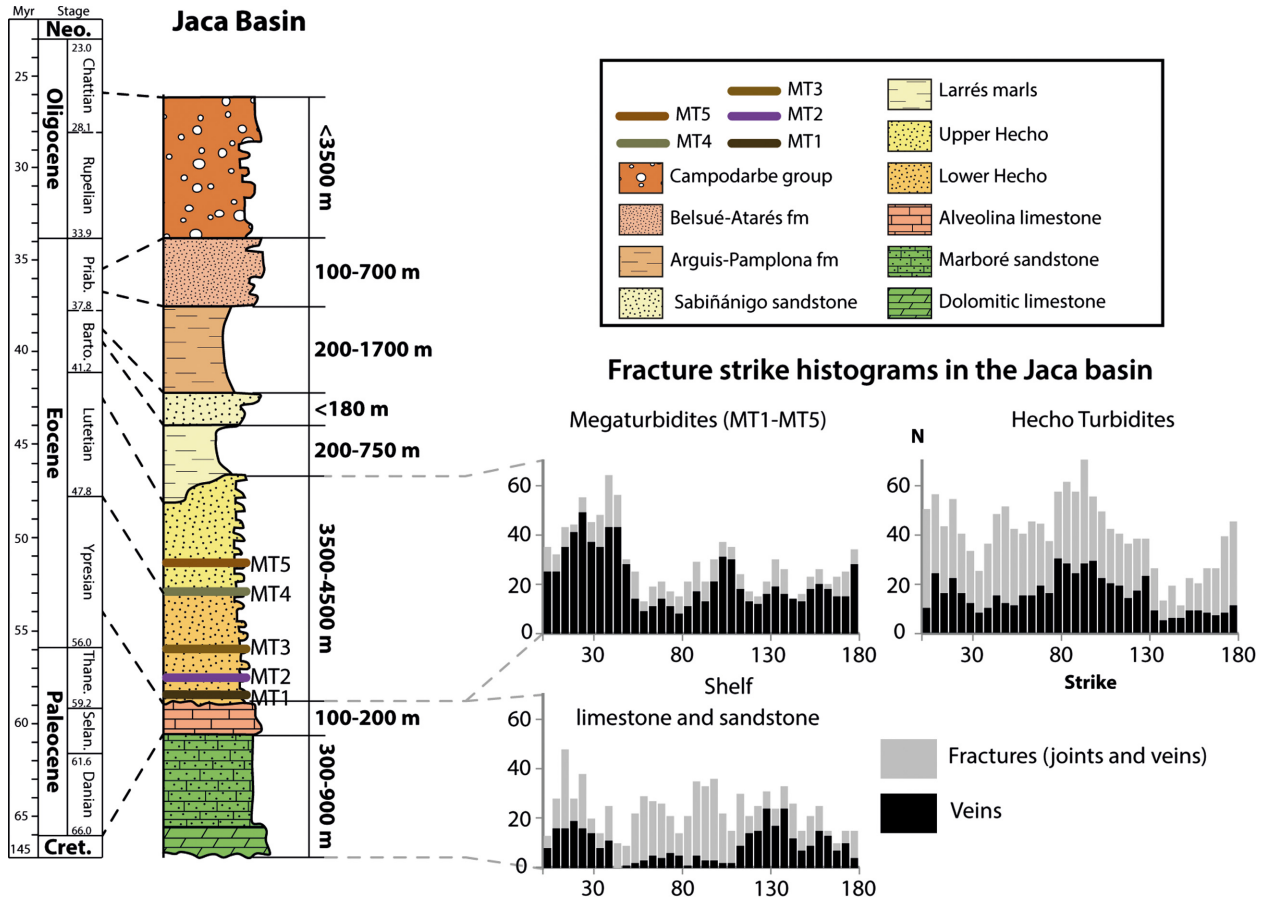


Fig. 3. Simplified sedimentary log of the Jaca basin (modified from Puigdefábregas (1975)) and fracture histograms of Eocene megaturbidites and turbidites and Cretaceous–Paleocene limestone and sandstone. Note the generalized infilling of fractures in the megaturbidites.

representative cluster to a fracture set and calculated the Fisher mean fracture pole at 95% level of confidence. To assess the relative chronology of fractures with respect to folding, poles of fractures are plotted both in geographic frame and after tilting back the bedding to the horizontal. Additional relative chronology among fracture sets was tentatively constrained by crosscutting or abutting relationships observed in the field.

Vein characterization

To study fluid–rock interactions, 108 veins and 83 associated host-rocks were sampled (Fig. 2). Vein texture analyses were carried out on 45 thin-sections using conventional optical microscopy and cathodoluminescence imaging using a CITL Cold Cathode Luminescence 8200 MK4 with an accelerating voltage of 12.5 kV and an intensity of 200–280 mA (LGCgE, University Lille 1 France). Images were acquired with a Spot Flex camera using an exposure time of up to 3 min due to the low luminescence of most cements.

O- and C-isotope compositions of samples were obtained by drilling out approximately 0.5 mg of sediment or minerals with a diamond bit. For samples located along the Torla valley (31 veins and 20 host-rocks), the isotopic compositions ($\delta^{18}\text{O}$ and $\delta^{13}\text{C}$) of carbonates were determined following method of Spötl & Vennemann (2003). CO_2 was produced from *ca.*250 μg of carbonate powder reacting with hydrochloric acid at 90 °C for 1 h. The produced CO_2 was removed with an helium stream and analysed using a Gas-Bench on a Finnigan MAT DeltaPlus XL mass spectrometer at the University of Lausanne (Switzerland). The results were corrected using the international standard NBS-19 and the analytical error was better than $\pm 0.05\text{‰}$ for $\delta^{13}\text{C}$ and $\pm 0.1\text{‰}$ for $\delta^{18}\text{O}$. For all other samples (77 veins and 63 host-rocks apart from the Torla valley), isotopic analysis was performed at the IStEP (Paris, France), using a Kiel IV Carbonate device connected to a mass spectrometer delta V advantage. About 40 μg of calcite powder was reacted with 104% phosphoric acid at 70 °C in individual vials. The CO_2 sample gas produced was purified in an automatic cryogenic system. Instrument calibration was

performed using the standard NBS 19 and an in-house standard (Marceau). The analytical precision determined by analysis of NBS 19 in association with sample was 0.07‰ for $\delta^{18}\text{O}$ and 0.03‰ for $\delta^{13}\text{C}$. Carbon and oxygen isotopic composition are reported as ‰ relative to Vienna Pee Dee Belemnite (VPDB).

Fluid-inclusion petrography was performed on 26 doubly polished thick sections (100 μm). Microthermometric analyses were performed on 21 selected thick sections using a Fluid Inc. USGS-type heating and freezing stage (LGCgE, University Lille 1, France) and a Linkam automatic THMSG600 cooling–heating stage (LFCR, Pau, France). Calibration of the microthermometric stages was made using synthetic fluid inclusions (SYNFLINC; (Sternner & Bodnar, 1984)) including, (i) pure water (ice melting temperature (T_m) = 0.0 °C; critical homogenization temperature (T_h) = 374.1 °C), (ii) $\text{H}_2\text{O}-\text{CO}_2$ inclusions (CO_2 melting temperature = -56.6 °C; hydrate melting temperature = +9.9 °C) and (iii) $\text{H}_2\text{O}-\text{NaCl}$ inclusions (eutectic temperature = -21.2 °C). Accuracy was ± 0.1 °C at temperature between -56.6 and +25 °C and ± 1.5 °C at +400 °C. After first progressively heating up to homogenization temperature (T_h), fluid inclusions were frozen and then slowly heated to determine eutectic temperatures (T_e) and the temperature of final melting of ice (T_m). NaCl-equivalent salinities (wt%) were calculated using the equation of (Bodnar, 1993). In order to evaluate the presence of volatile species in individual fluid inclusions (CH_4 , CO_2 , N_2 , H_2S), Raman spectra of individual fluid inclusions were recorded with a LabRam HR800 Jobin-Yvon microspectrometer equipped with 1800 g mm^{-1} gratings and using 532.28 nm (green) laser excitation (University Lille1, France). Acquisition time span varied from 20 to 60 s during three accumulating cycles.

RESULTS AND INTERPRETATIONS

Fracture network

We measured fractures in early syn-convergence deposits, namely late Cretaceous limestones and sandstones, Paleocene limestones and early Eocene Hecho turbidites, including limestones megaturbidites (Figs 3 and 4). The 48 sites are distributed from the Sierras Interiores (upper Cretaceous, Paleocene and Ypresian rocks) (17 sites) to the southern part of the turbiditic basin (mostly Lutetian rocks) (31 sites) (Figs 4–6). About two-third of fractures

(~65%) are perpendicular to bedding. Third (~31%) is oblique to bedding, and a small portion (~4%) is parallel to bedding. Note that ~6% of fractures are vertical in geographic frame and oblique to bedding. The fractures parallel to bedding are observed in the studied stratigraphic units but are more common in folded Eocene turbidites, at the interface between sandstones and marls. Generally, N–S slicken-slides are observed along these planes (Fig. 4h). Vertical fractures, oblique to bedding, range widely between N60–N170 and are observed only locally in megaturbidite 3 (unit MT3, Fig. 5) and in Eocene limestone near Sigues (sites E1 – E2, Figs 5 and 6).

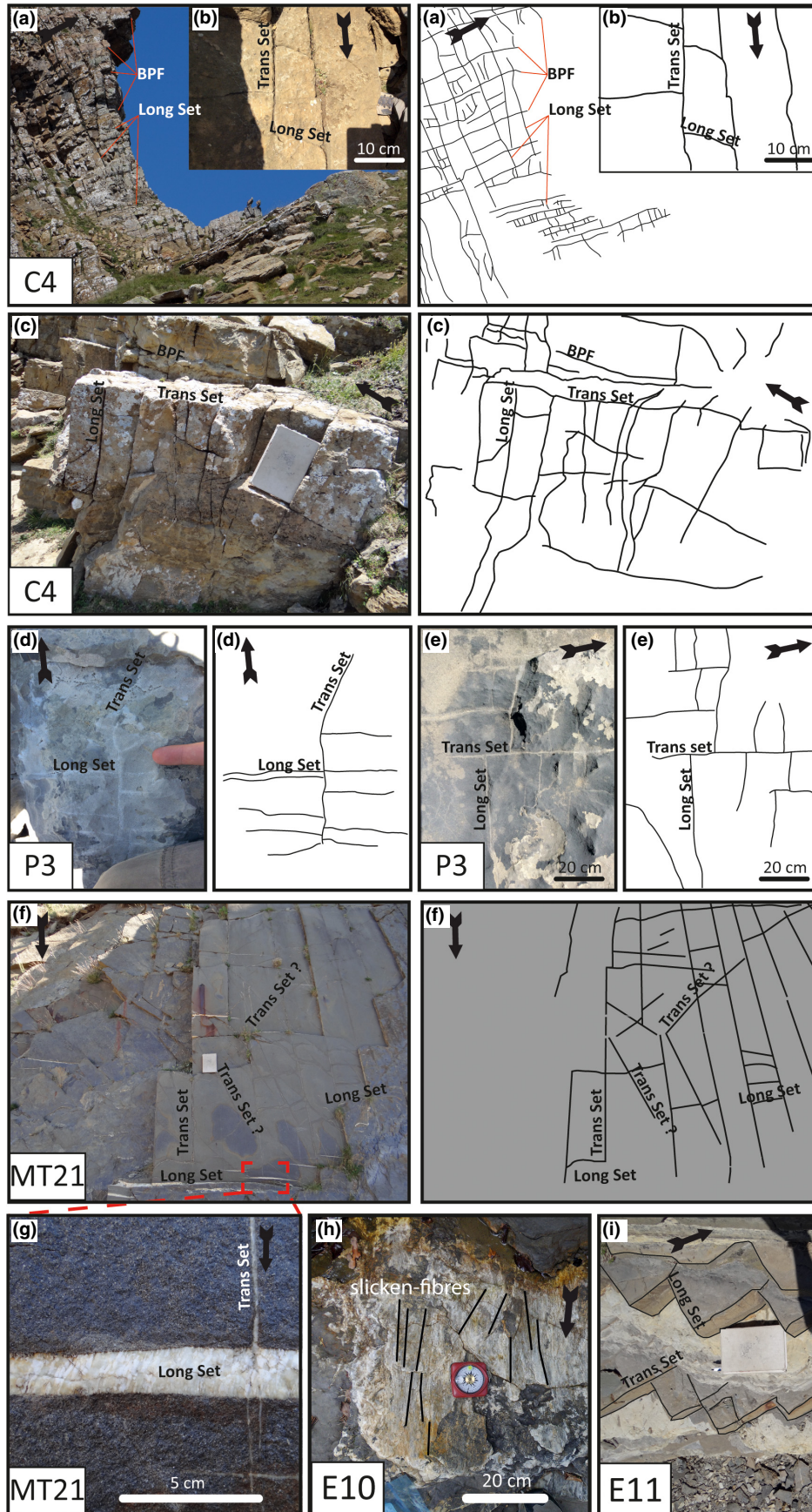
In this study, we focus essentially on fractures mostly perpendicular to bedding, which are by far the more numerous, and thus are considered as representative of the basin scale fracture network. In Cretaceous and Paleocene limestones and sandstones, the histogram of fracture orientation shows that the dominant fracture direction is ~N20 (Fig. 3). In Eocene turbidites, the dominant fracture orientation is ~N100. In folded foreland basin, it is generally conventional to name fracture longitudinal or transverse with respect to fold axes (e.g. Tavani *et al.*, 2015). In our study, we subsequently name longitudinal fractures when there are parallel to the $\text{N}100 \pm 30^\circ$ (fold axis trend) and transverse fractures when there are $\text{N}20 \pm 30^\circ$.

For transverse fractures, half of sites (24 of 48 sites) displays one transverse set, while other sites exhibit up to three fracture sets, as for example in megaturbidite 2 (site MT21) (Fig. 4f). In this site these transverse fractures strike N05, N30 and N140 after bedding correction (Fig. 4d,f). These orientations are close to those observed in older rocks from the same area (Fig. 6): N10–N20 in the upper Cretaceous (site C4), N20–N25 in the Paleocene (site P3), N15 and N140 in megaturbidite 1 (site MT11), N20 and N170 in megaturbidite 3 (site MT33).

For longitudinal fractures, almost 80% of sites display one or two longitudinal fracture sets (Figs 4–7). Other sites display up to three main fracture sets. Longitudinal fractures mostly strike between N70 and N130. For example, in the Ansó area, longitudinal sets strike N120 in the upper Cretaceous (site C4), N120, N130 and N145 in the Paleocene (site P3), N115 in megaturbidite 1 (site MT11), N100 in megaturbidite 2 (site MT21) and N125 in megaturbidite 3 (site MT33) (Figs 4–7).

These observations highlight that, at first glance, and despite a quite complex fracturing network, orientations of transverse and longitudinal fractures are consistent

Fig. 4. Field photographs of fracture networks. (a, b, c) bed-perpendicular and bed-parallel fractures in upper Cretaceous sandstone (site C4). (d, e) bed-perpendicular fractures in Paleocene limestone (site P3). (f) bed-perpendicular fractures in megaturbidite MT2 (site MT21). (g) mineralized longitudinal fracture showing fibrous calcite; extensional vein (site MT21). (h) Slicken-fibres of a shear vein (site E10). (i) bed-perpendicular fractures in turbiditic sandstone (site E11). (b, d, e, f) abutting relationships (sites C4 and P3). See location of sites in Fig. 6.



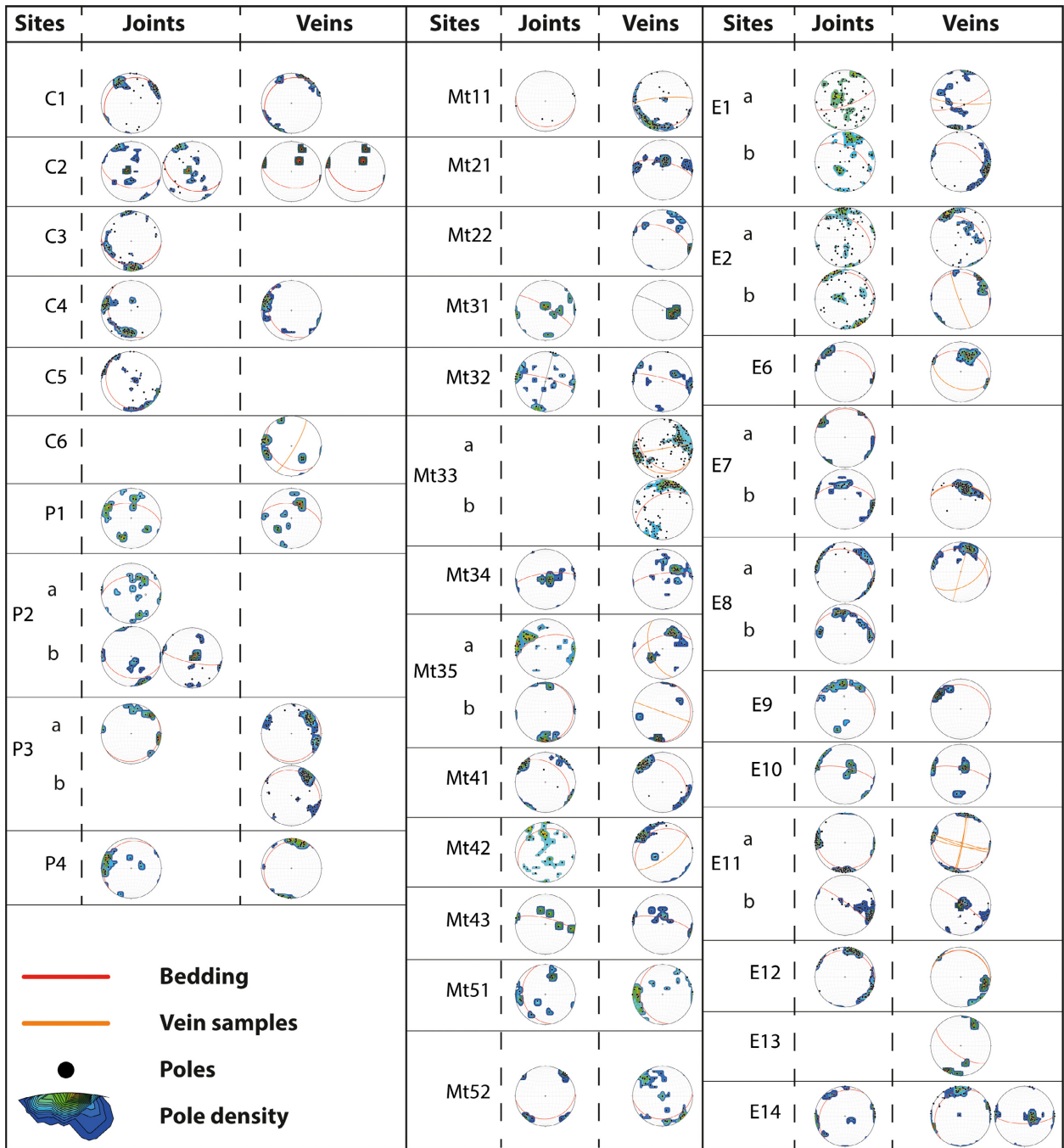


Fig. 5. Results of fracture analysis in Cretaceous to upper Eocene syn-tectonic strata. Results are presented on Schmidt's lower-hemisphere, equal-area stereonets, and display raw data in current strata attitude for both joints (left) and veins (right).

between sites of different age, lithology and structural position.

We plot the representative transverse and longitudinal fracture sets at the basin scale (Fig. 6). Transverse fracture sets are homogeneous in the eastern part of the basin. They are more scattered in the western part of the basin. Apart few exceptions, longitudinal fractures are also homogeneous at the scale of the basin (Fig. 7).

The chronology of fracturing between transverse and longitudinal fractures has been determined in five sites from upper Cretaceous, Paleocene, and Lutetian deposits of the Sierras Interiores (sites C4, C6, P3, MT21 and E8; Fig. 4). They display reliable chronology of fracturing among transverse fractures (one site in Lutetian Hecho turbidites; site E8) and between transverse and longitudinal fractures (five sites in

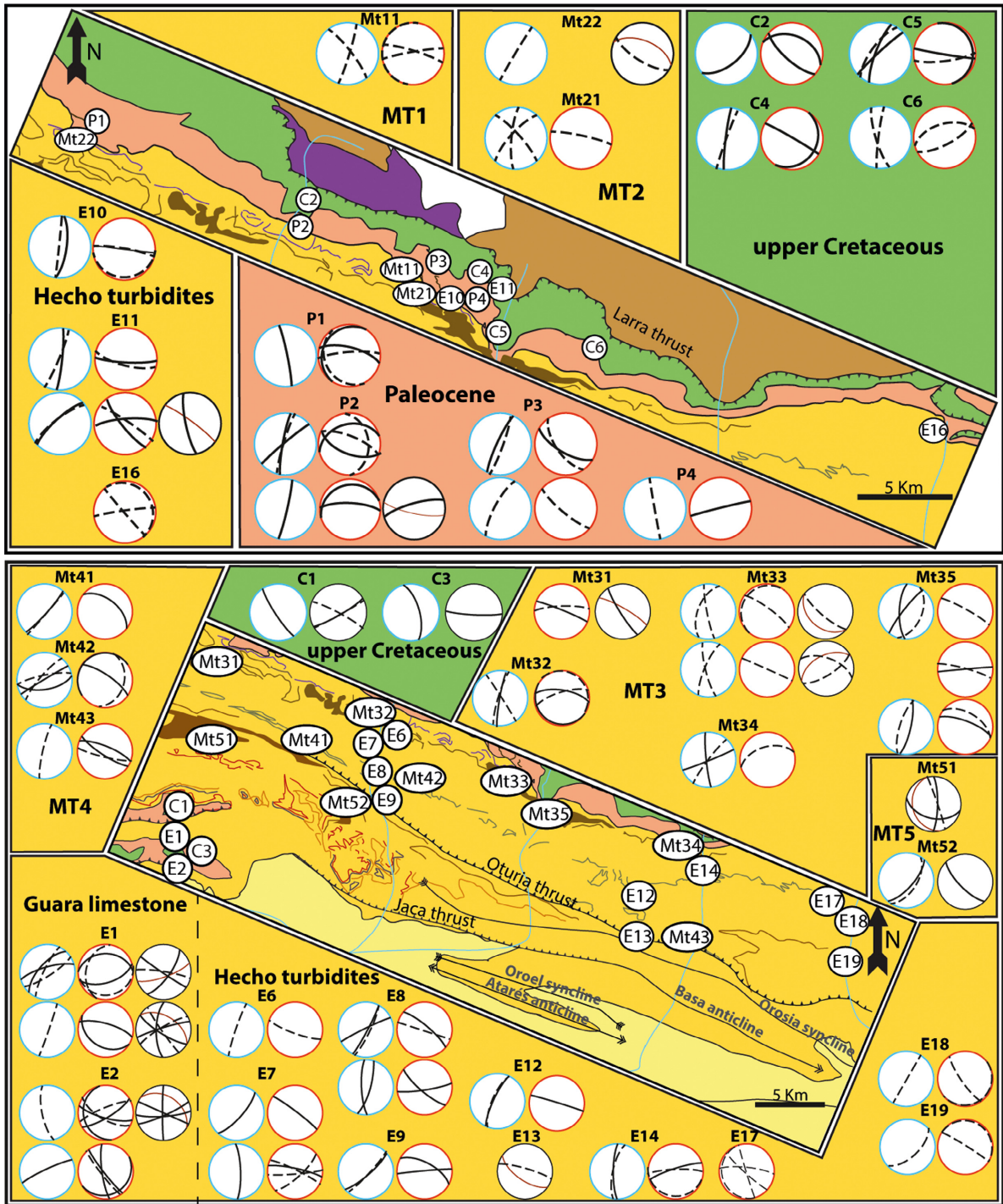


Fig. 6. Simplified results of fracture analysis in upper Cretaceous to upper Eocene strata. Results are presented on three diagrams (Schmidt' lower hemisphere, equal-area stereonets) displaying data corrected for local bedding dip (left blue and middle red) and in current strata attitude (right dark). Blue diagrams represent transverse fracture sets and red diagrams represent longitudinal and bed-parallel fracture sets. Black diagrams represent vertical in-situ and oblique to bedding fracture sets (bedding in red). Dashed black lines are veins. See Fig. 2 for key of geological map.

upper Cretaceous, Paleocene, Lutetian Hecho turbidite and megaturbidite deposits of the Sierras Interiores; sites C4, C6, P3, MT21 and E8). In the Lutetian

turbidites of the Hecho valley (site E8) abutting relationship among transverse fractures are equivocal and do not allow to clearly assess chronology. However,

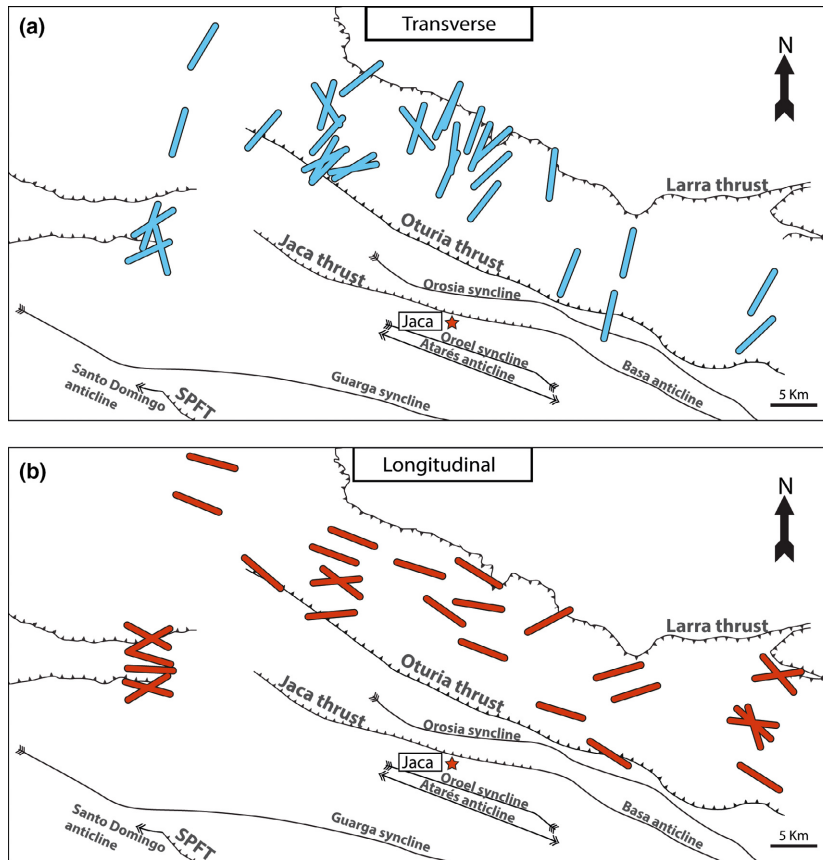


Fig. 7. Regional fracture network map showing the distribution and orientation of the two main fracture sets in the Jaca basin. (a) The N-S (blue) and (b) E-W (red) sets are corrected from local bedding. SPFT: South Pyrenean Frontal Thrust.

abutting relationships suggest that longitudinal fractures post-dated transverse fractures. The same trend was observed in the four other sites (Figs 4b,d,e and 6).

Vein network and texture analysis

Vein network

In the study area, about half of fractures (52%) are mineralized (Fig. 3). These veins are observed in 80% of measurement sites (34 of 48 sites) (Figs 4f and 6). In late Cretaceous and Paleocene carbonates, veins are poorly represented (<10% of fractures) in longitudinal-like fractures. In Eocene turbidites, veins represent about 30% of fractures whatever their orientation. In

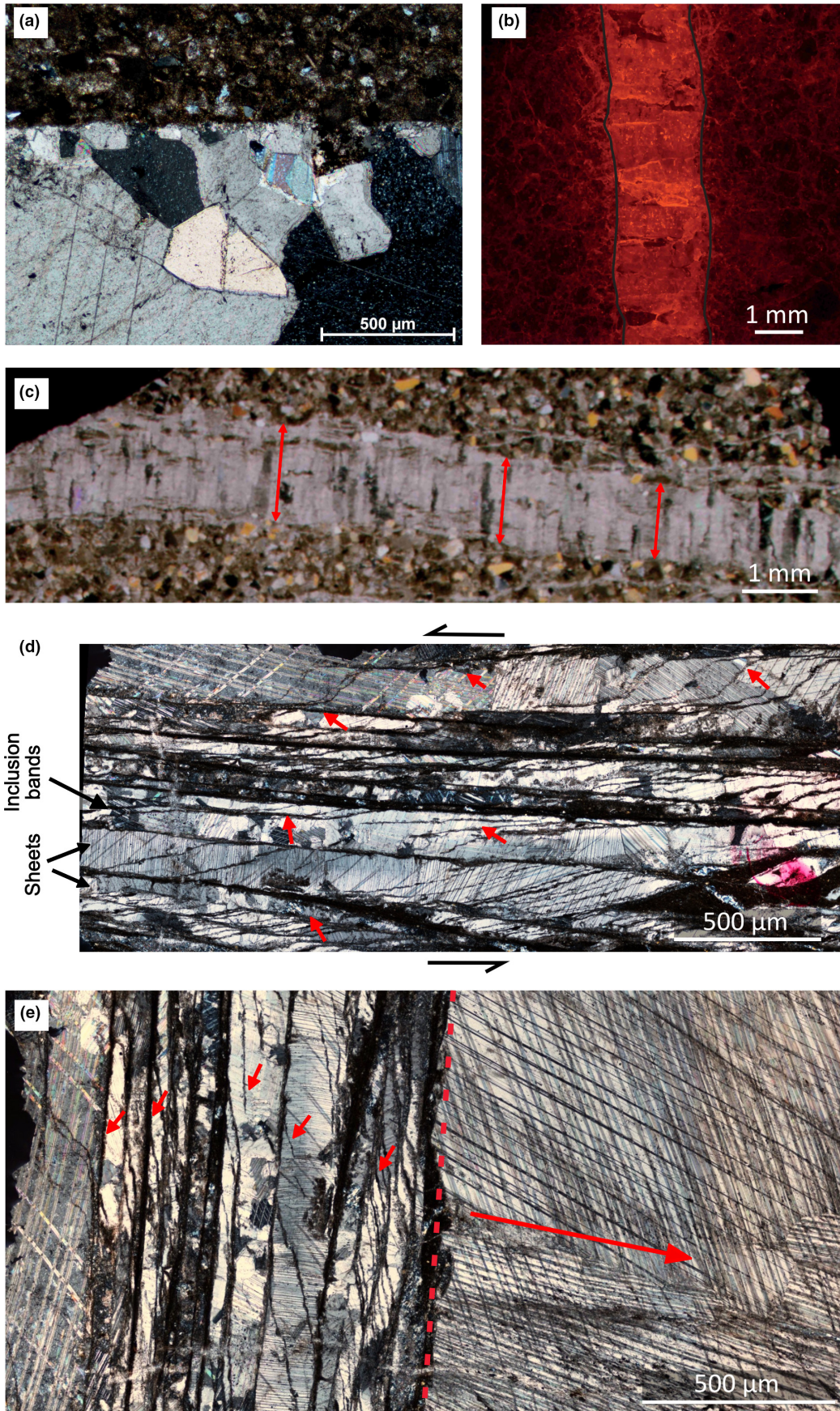
carbonate megaturbidites (MT1 to MT5), veins fill more than 60% of fractures irrespective of their orientation (Fig. 3).

Vein petrography

Veins are characterized by their crystal morphologies (e.g. blocky, elongate blocky, fibrous), their growth direction (syntaxial or antitaxial) and their opening mode (shear veins vs. extensional veins, hereafter referred respectively as SV and EV) (Bons *et al.*, 2012).

Extensional veins are millimetre to centimetre-thick. They extend over several centimetres to decametres (Fig. 8a,b). They are composed of blocky to elongated-blocky calcite crystals, whose C-axis is sub-perpendicular

Fig. 8. Photomicrographs of extensional veins (EV) and SV-EV calcite veins. (a) Example of blocky calcite in an extensional vein. (b) Cathodoluminescence photomicrograph of elongated blocky calcite with homogeneous dull orange luminescence. (c) Example of elongated calcite in an extensional vein. The red arrows indicate the direction of growth of the calcite crystals. (d) Detail of the crack-seal zone of a SV-EV vein (equivalent to a shear vein). The red arrows indicate the sense of growth of individual calcite crystals. (e) Example of SV-EV vein with a crack-seal zone on the border and blocky calcite in the centre (left and right of the dotted line respectively). The red arrows indicate the sense of growth of individual calcite crystals.



to vein borders, supporting syntaxial mode-I opening (Bons *et al.*, 2012) (Fig. 8a,b). They can present evidence of multiple crack-sealing events (Fig. 8c). In some veins, quartz crystals are imbricated with calcite, and are inferred to be cogenetic with calcite. Calcite always presents homogeneous dull orange luminescence in CL (Fig. 8b).

Shear veins correspond to millimetre to centimetre-thick alternations of calcite and host-rocks sheets, parallel to the macroscopic vein and featuring striped or fibrous appearance (slicken fibres) (Fig. 4h). Under the optical microscope, the calcite sheets consist of an alternation of sub-millimetric rhomb-shaped calcite increments delimited by thin oblique inclusion trails. Individual calcite crystals are oblique to the vein walls, and can encompass several calcite increments (Fig. 8d). Based on Bons *et al.* (2012) and Passchier & Trouw (2006), the calcite increments are interpreted as pull-apart openings formed during successive crack-seal events, in a shear vein with small jogs. All calcite crystals have homogeneous dull orange luminescence in CL. Some veins (labelled as SV-EV) show both characteristics of shear veins and extensional veins, with alternations of calcite and host-rocks slices on their borders (equivalent to SV), and a centimetre-wide zone filled by blocky calcite (locally with minor quartz) in their centre (equivalent to EV) (Fig. 8e). At site C4, the centre of SV-EV veins is locally empty. Such textures strongly suggest transition from mode II (shear) to mode I (extensional), and thus reflect at least two distinct precipitation stages.

Stable isotopes

Stable isotope analyses have been performed on 81 bulk rocks and 88 veins (Fig. 9a–d; corresponding table is available in Table S2), corresponding to 37 EV, 5 SV and 46 SV-EV veins. Veins correspond equally to transverse fractures (23), longitudinal fractures (37) and bed-parallel fractures (20). Few veins fill vertical fractures (8). For SV-EV veins, isotope results have been mostly acquired on blocky calcite (EV zone) rather than thin crack-seal zones (SV zone), owing to the absence of host-rock slices.

In veins within upper Cretaceous carbonates, $\delta^{13}\text{C}$ and $\delta^{18}\text{O}$ range from 0.0 to +2.0‰ and from –6.0 to –10.0‰ respectively ($n = 5$). Host-rock display $\delta^{13}\text{C}$ and $\delta^{18}\text{O}$ from +0.7 to +2.2‰ and from –8.9 to –4.8‰ respectively ($n = 5$) (Fig. 9a).

In veins within Paleocene limestones and early Eocene limestones/marls, $\delta^{13}\text{C}$ and $\delta^{18}\text{O}$ range from –8.1 to

+2.5‰ and from –20.2 to –4.2‰, respectively ($n = 10$). Host-rock display $\delta^{13}\text{C}$ and $\delta^{18}\text{O}$ from –5.8 to +3.1‰ and from –16.9 to –2.4‰ respectively ($n = 10$) (Fig. 9a).

In veins from Eocene turbidites and megaturbidites, $\delta^{13}\text{C}$ and $\delta^{18}\text{O}$ range from –9.0 to +2.0‰ and from –17.0 to –3.0‰, respectively ($n = 88$). Host-rock display $\delta^{13}\text{C}$ and $\delta^{18}\text{O}$ range from –8.6 to +3.0‰ and from –14.5 and –2.4‰, respectively ($n = 64$) (Fig. 9a).

In veins from upper Eocene marls, $\delta^{13}\text{C}$ and $\delta^{18}\text{O}$ range from –5.0 to +13.0‰ and from –11.0 to –5.0‰ respectively ($n = 4$). Host-rock display $\delta^{13}\text{C}$ and $\delta^{18}\text{O}$ from –0.1 to +0.5‰ and from –5.6 to –5.2‰ respectively ($n = 2$) (Fig. 9a).

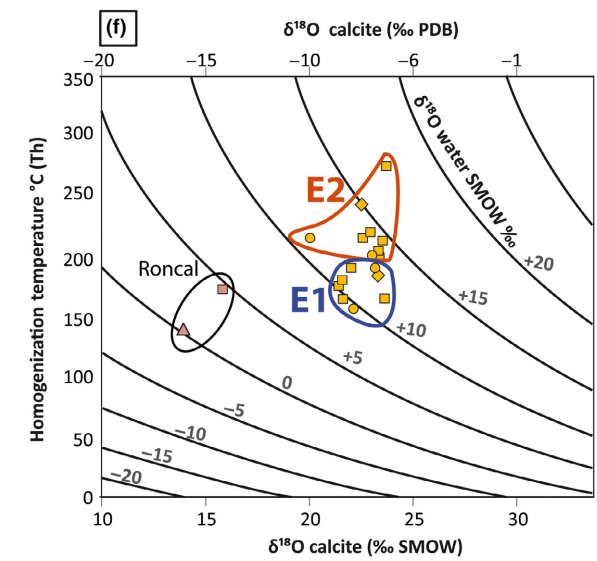
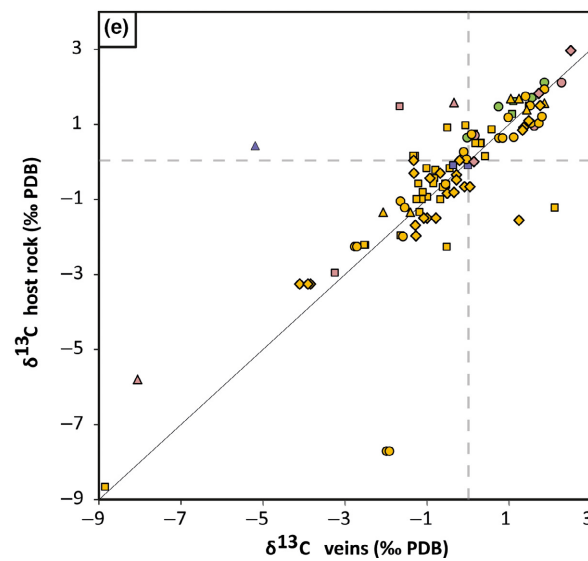
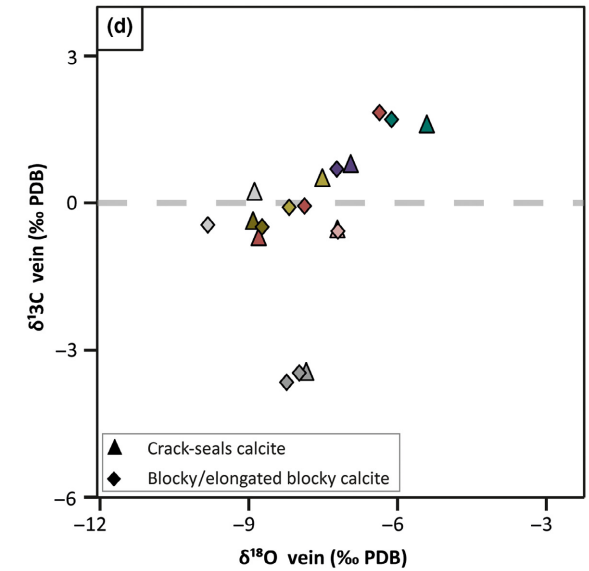
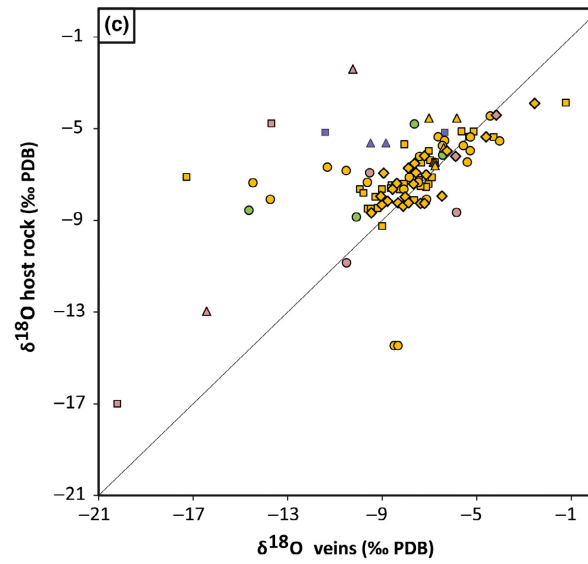
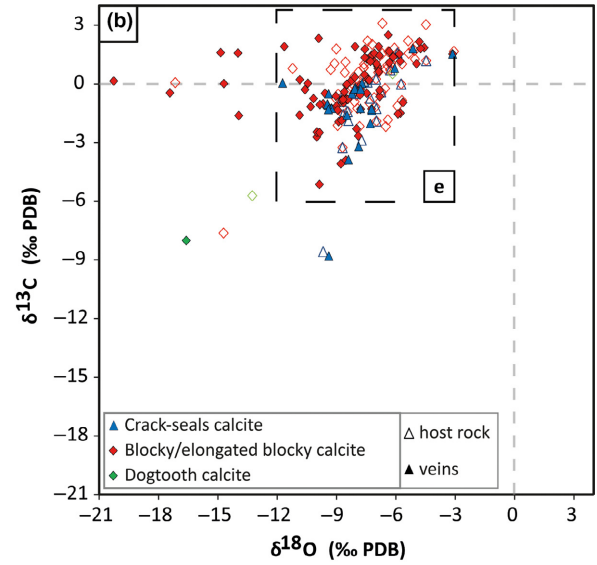
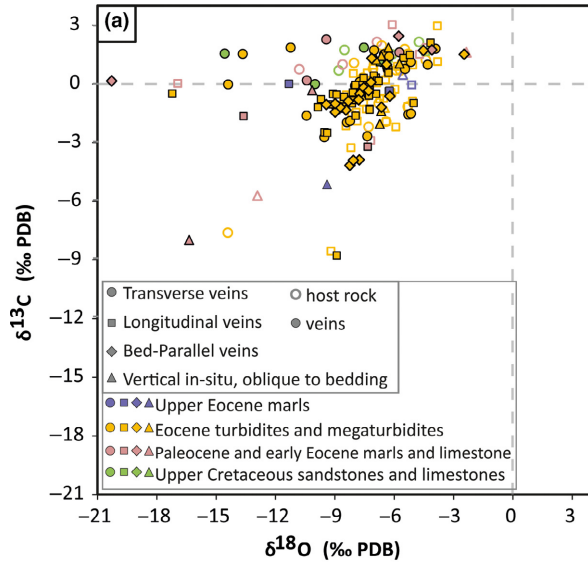
Stable isotope analyses of EV and SV show no difference depending on the opening mode (shear vs. extension) (Fig. 9d). In SV-EV samples where stable isotope analyses were performed both on crack-seals and blocky calcite ($n = 8$), we observed no difference according to opening mode (Fig. 9e).

It turns out that 74% of veins exhibit the same C and O isotopic composition than their host rock (Fig. 9a–d) whatever their striking and opening mode (Fig. 9e). For the other veins, the difference of isotopic composition can reach up to 10.0‰ for $\delta^{18}\text{O}$ and 12.7‰ for $\delta^{13}\text{C}$ with respect to host rocks. Such pattern is mostly observed in veins from the south of the Roncal valley (six veins) and in Eocene turbidites (14 veins), regardless their opening type and orientation (Fig. 9).

Fluid inclusion petrography

Primary and secondary fluid inclusions (Fig. 10) were studied in 14 veins from the Sierras Interiores and 12 veins from the turbiditic basin, corresponding to 13 EV and 13 SV-EV veins (Figs 11 and 12) (Table 1). These veins are located mostly to the north of the Jaca basin, in the Torla and Aragües valleys (B2–B6; A1; A2; Fig. 12), within the core of turbiditic through in the Torla valley and the Hecho valley (B1; H1–H3; Fig. 12) or localized at the southern border of the turbiditic through along the Roncal valley (R1; R2 Fig. 12). Four veins are parallel to transverse fractures (three EV and one SV-EV), 15 to longitudinal fractures (seven EV and eight SV-EV), six to bedding-parallel fractures (two EV and four SV-EV) and one to a vertical in-situ fracture (one EV) (Table 1). A total of 254 fluid inclusions were studied in calcite

Fig. 9. Results of oxygen and carbon isotopic analyses of veins and host-rocks for the entire study zone. (a) Cross-plot of the oxygen and carbon isotopic data sorted by fracture orientation and age of host-rocks. (b) Cross-plot of the vein oxygen and host-rock oxygen isotopic data. (c) Cross-plot of the vein carbon and host-rock carbon isotopic data. (d) Cross-plot of the oxygen and carbon isotopic data sorted by vein texture. (e) Zoom of (d) showing isotopic results for different textures in a same vein. Each colour refers to one vein. (f) Isotopic composition of water calculated from oxygen isotope data and homogenization temperatures, using the equation from Friedman & O'Neil (1977). Curve lines correspond to fluid isopleths. E1 and E2 correspond to vein precipitation stages 1 and 2 respectively (see text for details).



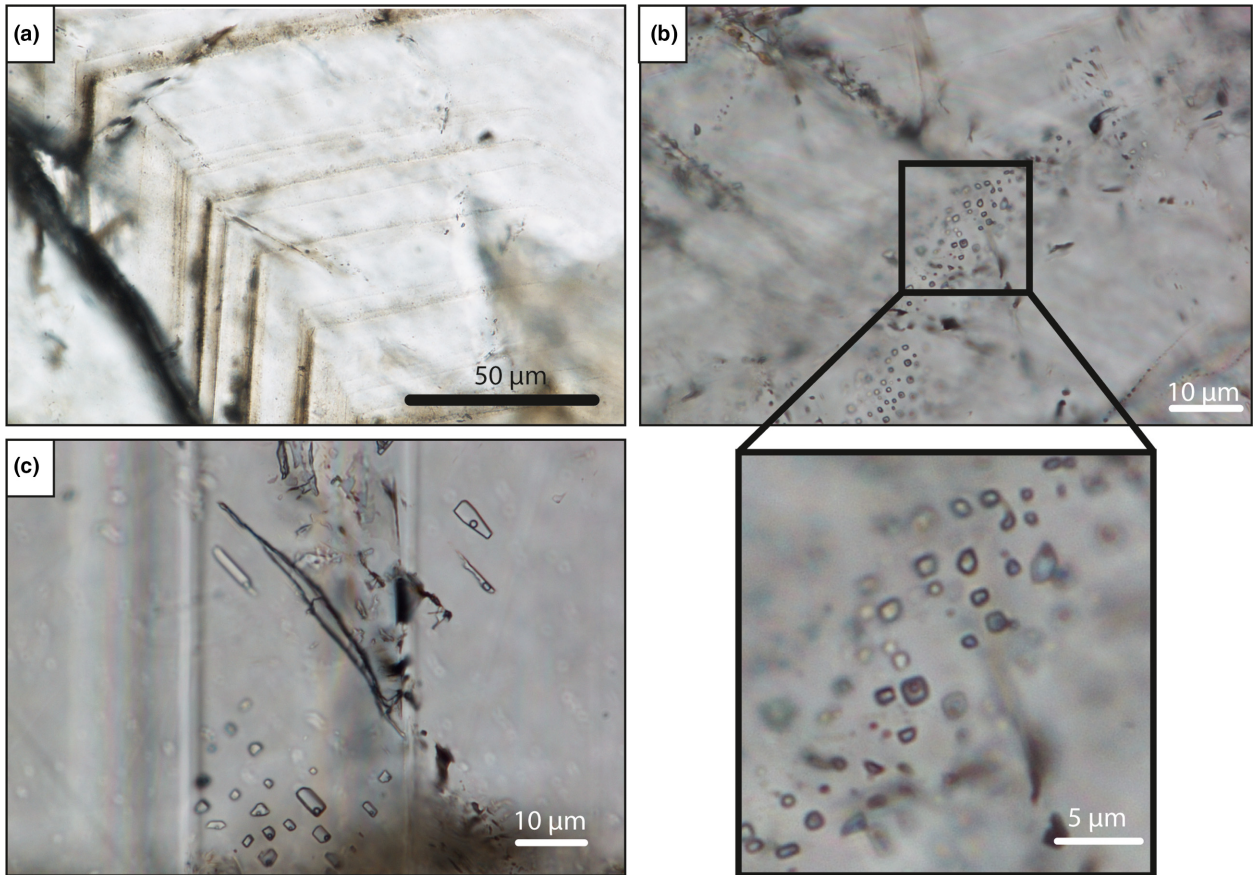


Fig. 10. Microphotographs of fluid inclusions. (a) Primary fluid inclusions defining crystal growth zonations in calcite. (b) Small secondary fluid inclusions in calcite. (c) Detail of primary fluid inclusions showing homogeneous fluid/gas ratio.

($n = 197$) and quartz crystals ($n = 57$) (Figs 10–12) (Table 1). Primary fluid inclusions (192 of 254) were identified both by their occurrence in alternating inclusion-rich and inclusion-poor crystal growth bands (Fig. 10a) and by their preferential orientation and shape in the growth direction of calcite and quartz (e.g. Goldstein, 2001). They are commonly isolated, but locally form clusters of ~ 10 fluid inclusions which vary between 3 and 8 μm in size, and define a fluid inclusion assemblage (FIA; Goldstein & Reynolds (1994)). For a given FIA, the ratio between the vapour and the liquid (V/L) remains mostly consistent. Secondary aqueous fluid inclusions are generally small ($< 5 \mu\text{m}$), rounded in shape and aligned along fractures planes. Only inclusions bigger than *ca.* 3 μm are able to be identified as two-phases, with a V/L ratio mostly constant. A total of 60 FIA (46 primary and 14 secondary) are considered in the dataset.

Microthermometry and Raman spectroscopy on fluid inclusions

Only 21 veins contain fluid inclusions suitable for microthermometric analyses (size higher than *ca.* 3 μm)

(Table 1). Due to the small size of most inclusions ($< 5 \mu\text{m}$), eutectic temperatures (T_e) could be measured reliably in 3 EV and 2 SV-EV veins only. They vary between $-23.5 \text{ }^\circ\text{C}$ and $-21.5 \text{ }^\circ\text{C}$, which is characteristic of the H_2O – NaCl system (Goldstein, 2001). A total of 208 homogenization temperatures (T_h) and 161 melting temperatures of ice (T_m) were measured in primary and secondary FIAs. Because calcite and quartz exhibit overlapping T_h and T_m values in a same vein, microthermometric data are presented without consideration of the host mineral (Figs 11 and 12).

In extensional veins (EV), the range of T_h and T_m of primary aqueous fluid inclusions is large ($T_h = 126 \text{ }^\circ\text{C}$ to $280 \text{ }^\circ\text{C}$; $T_m = 0$ – $-4.9 \text{ }^\circ\text{C}$, corresponding to salinities of 0–7.7 wt% eq. NaCl). For secondary fluid inclusions, this is about the same pattern ($T_h = 160$ – $265 \text{ }^\circ\text{C}$; $T_m = -0.9$ – $-4.2 \text{ }^\circ\text{C}$, corresponding to salinities of 1.6–6.7 wt% eq. NaCl) (Fig. 11) (Table 1). Within FIAs, the distribution (difference between maximum and minimum) of T_h and T_m is narrow, generally within 20 and 0.9 $^\circ\text{C}$ respectively (Figure S1). However, in the Torla, Aragón and Hecho valleys, a bimodal distribution of T_h and T_m is observed in individual primary FIAs (Fig. 13).

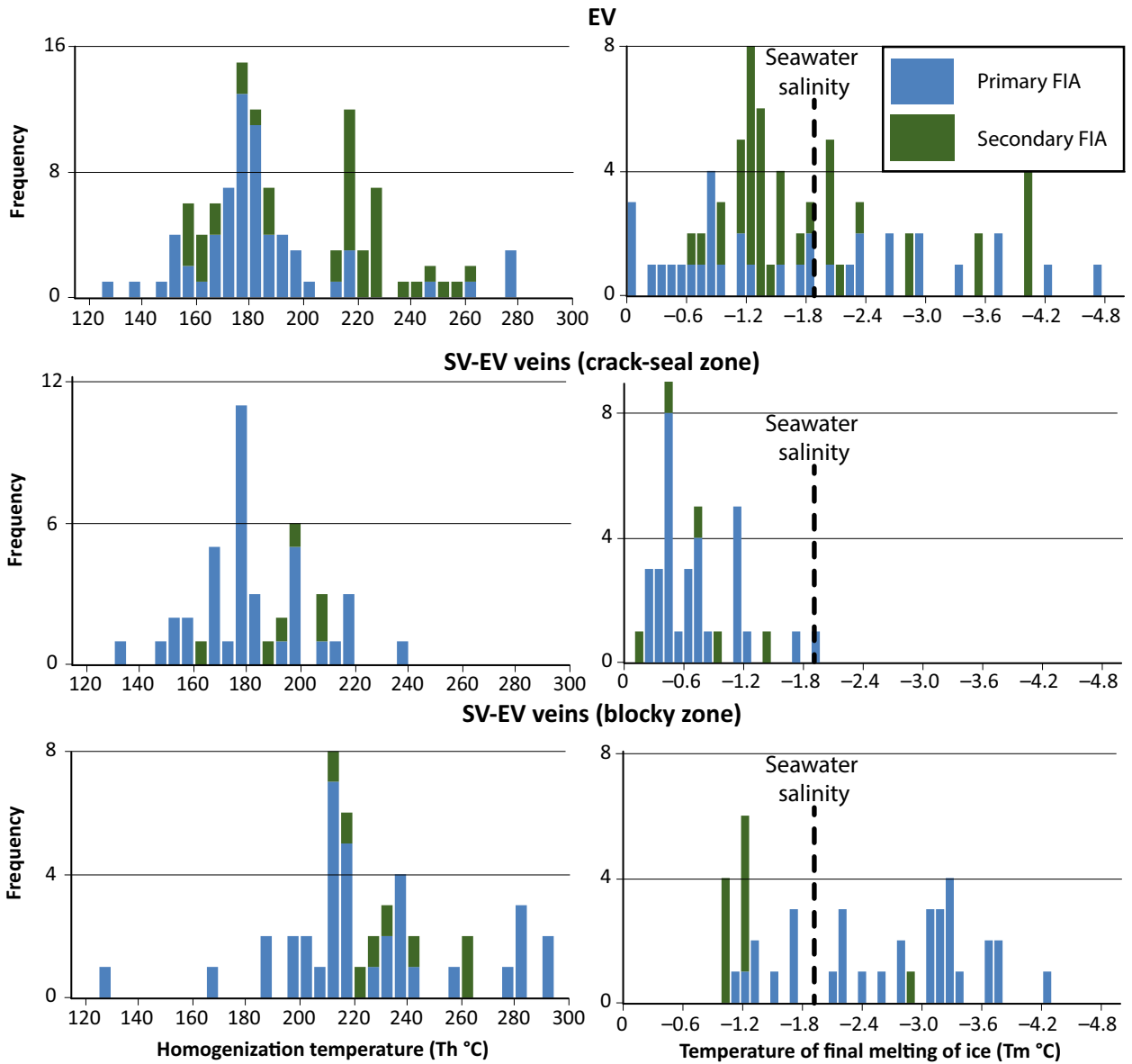


Fig. 11. Frequency plots of homogenization temperatures (T_h) and temperature of final melting of ice (T_m) of primary (blue) and secondary (green) fluid inclusions. EV: extensional veins. SV-EV veins (crack-seal zone): border of SV-EV veins. SV-EV veins (blocky zone): centre of SV-EV veins.

This distribution suggests partial overheating (i.e. stretching), and/or leakage and refilling (e.g. Goldstein, 2001). In one sample from the Torla valley (To11-09 EV1), microthermometric analyses of one-phase bigger, dark fluid inclusions highlighted the presence of methane ($T_h = -82.6$ – -82.9 , mode = -82.7 °C) (Fig. 14a,b). Furthermore, Raman spectroscopy performed on this sample (5 one-phase, dark fluid inclusions and 4 two-phase fluid inclusions from the same FIA) confirmed the presence of methane (Raman peak at about 2915 cm^{-1}).

In SV-EV veins, we distinguish crack-seal zones and blocky zones. In crack seal zones, T_h and T_m of primary

FIs range from 135 to 240 °C and -0.3 to -1.9 °C (salinity of 0.5 – 3.2 wt% eq. NaCl) respectively. In blocky zones, T_h and T_m range from 130 to 294 °C and -1.1 to -4.4 °C (salinity of 1.9 – 7.0 wt% eq. NaCl) respectively (Figs 11–13) (Table 1). In a single vein, T_h and T_m of primary FIAs differ between crack-seal and blocky zones, with higher T_h and lower T_m in the blocky zone (Figs 10 and 11). For secondary fluid inclusions, T_h and T_m values of crack-seal zones are in the range 164 – 210 °C and -0.3 – -1.3 °C (salinity of 0.5 – 2.2 wt% eq. NaCl), respectively. They are more restricted in blocky zones, with values of 215 – 260 °C and -1 – -3 °C (salinity

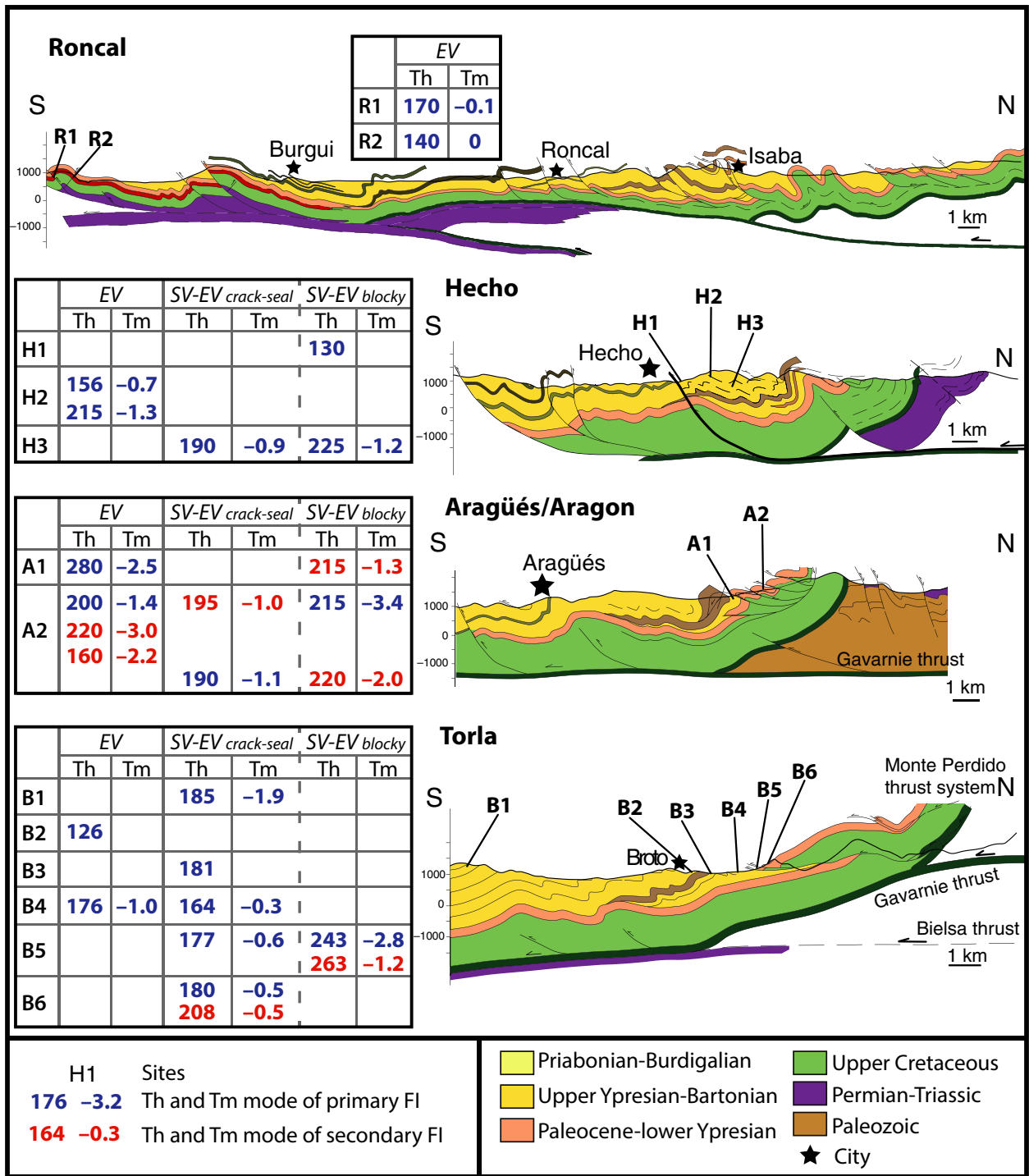


Fig. 12. Location of microthermometric results along four N-S cross-sections modified from Izquierdo-Llavall *et al.* (2013). Results are presented according to the type of veins (EV, SV-EV) and of fluid inclusions (primary in blue and secondary in red). See Fig. 2 for the location of cross-sections.

of 1.7–5.0 wt% eq. NaCl) respectively (Fig. 11) (Table 1).

For the crack-seal zone, within individual FIAs, the variability range of Th and Tm is generally around 24 and 0.7 °C respectively (12 FIAs), except in the Torla

valley where the variability is higher (Table 1). For the blocky zone, within individual FIAs, the variability range of Th and Tm is generally around 30 and 0.7 °C respectively (13 FIAs). In the blocky zone of one vein of the Hecho valley (HH14/05 EV2), microthermometric

Table 1. Synthesis of microthermometric results

Sites	Sample names	Vein texture	Fracture set	FI types	T _m mode (°C)	n	T _m min/max	Leakage/ refilling	Th mode (°C)	n	Th min/max	Overheating
R1	RO14-07 01	EV	Longitudinal	I	-0.1	7	-0.5/0	No	170	9	160–180	No
R2	RO14-07 02	EV	Vertical in-situ	I	0	1	n	No	140	1	n	No
H1	HH14-04 SV	SV-EV blocky	Bed-parallel	I	n	0	n	No	130	1	n	No
H2	HH14-05 EV1	EV	Transverse	I	-0.7	4	-0.9/-0.4	no	156	5	150–183	Yes
H2	HH14-05 EV2	EV	Transverse	I	-1.3	9	-1.7/-0.7	No	215	9	180–220	No
H3	HH14-10 EV1	SV-EV crack-seal	Longitudinal	I	-0.9	5	-1.2/-0.2	No	190	4	170–200	No
H3	HH14-10 EV1	SV-EV blocky	Longitudinal	I	-1.2	2	-3.3/-1.2	No	225	6	190–240	No
A1	JA13/23/10/13 bis	EV	Longitudinal	I	-2.5	3	-2.5/-2.4	No	280	4	265–280	No
A1	JA13/24/10/01	SV-EV blocky	Longitudinal	II	-1.3	6	-3/-1.3	No	215	6	215–235	No
A2	JA13/23/10/05	SV-EV crack-seal	Transverse	I	-1.1	2	-1.3/-1	No	190	14	180–200	No
A2	JA13/23/10/05	SV-EV blocky	Transverse	II	-2	3	-2/-1	No	220	1	No	No
A2	JA13/23/10/03	EV	Transverse	I	-1.4	22	-2/-1.1	No	200	25	185–265	Yes
A2	JA13/23/10/11	EV	Longitudinal	II	-3	2	n	No	220	2	n	No
A2	JA13/23/10/10	EV	Longitudinal	II	-2.2	6	-2.5/-2.2	No	160	6	160–170	No
A2	JA13/23/10/10bfc	SV-EV blocky	Longitudinal	I	-3.4	6	-3.8/-3.3	No	215	12	190–220	No
A2	JA13/23/10/09	SV-EV crack-seal	Longitudinal	I	-1	3	-1.5/-0.8	No	195	4	190–210	No
B1	BR 11-04 SV	SV-EV crack-seal	Bed-parallel	I	-1.9	1	n	No	185	3	170–197	No
B2	BR 11-01 SV	EV	Bed-parallel	I	n	0	n	No	126	1	n	No
B3	TO 11-12 SV2	SV-EV crack-seal	Bed-parallel	I	n	0	n	No	181	1	n	No
B4	TO 11-09 SV1	SV-EV crack-seal	Longitudinal	I	-0.3	1	n	No	164	7	135–164	No
B4	TO 11-09 EV1	EV	Longitudinal	I	-1	35	-4.9/-0.2	Yes	176	31	151–246	Yes
B5	TO 11-05 SV	SV-EV crack-seal	Bed-parallel	I	-0.6	7	-1.3/-0.2	No	177	7	175–182	No
B5	TO 11-05 SV	SV-EV blocky	Bed-parallel	I	-2.8	23	-4.4/-1.2	No	243	13	202–293	Yes
B5	TO 11-05 SV	SV-EV blocky	Bed-parallel	II	-1.2	4	-1.3/-1.1	No	263	3	242–263	No
B6	TO 11-02 SV	SV-EV crack-seal	Longitudinal	I	-0.5	9	-0.6/-0.2	No	180	8	170–195	No
B6	TO 11-02 SV	SV-EV crack-seal	Longitudinal	II	-0.5	13	-2/-0.4	No	208	11	200–235	No

EV, extensional veins; SV-EV, veins showing both shear and extensional zones; T_m, temperature of final melting of ice; Th, homogenization temperature; n, not determined.

analyses of one-phase big, dark fluid inclusions highlighted the presence of methane ($T_h = -83.7$ – 84.3 , mode of -84 °C) (Fig. 14b). Raman spectroscopy performed on this sample (5 one-phase, dark fluid inclusions and 3 two-phase fluid inclusions from the same FIA) confirmed the presence of methane.

The simultaneous presence in a defined FIA, of methane and of two-phase aqueous fluid inclusions showing various V/L ratios (samples TO11/09 EV1 and HH14/05 EV2) (Fig. 14c), suggests heterogeneous entrapment of two immiscible fluid phases (H_2O and CH_4) (Goldstein & Reynolds, 1994).

DISCUSSION

Conditions and timing of fracture development

Fractures networks of foreland settings can either be inherited from former orogenic episodes of deformations, developed during early compression by layer parallel shortening (LPS), or during further sediment burial stages (Engelder & Peacock, 2001; Bergbauer & Pollard, 2004; Bellahsen *et al.*, 2006; Tavani *et al.*, 2006; Branellec *et al.*, 2015). In our study, fractures originated from Pyrenean orogeny because studied rocks are syn-orogenic (upper Cretaceous to upper Eocene).

Tavani *et al.* (2015) proposed that the pattern of transverse and longitudinal fractures can be related to Layer Parallel Shortening (LPS) followed by folding. LPS is widely recognized in foreland basin and fold-and-thrust belts (e.g. Bellahsen *et al.*, 2006; Beaudoin *et al.*, 2011; Branellec *et al.*, 2015). In response to LPS, transverse fractures develop before and during early folding. Then, longitudinal fractures can easily develop during development of thrust-related anticlines (Tavani *et al.*, 2015). Sticking to the hypothesis that transverse fractures observed in the Jaca Basin are related to LPS, we propose that these fractures formed essentially before thrusting events (*ca.* 44 My in the Sierras Interiores, and *ca.* 38 My in the turbiditic basin; Labaume *et al.* (2016)). The orientation of transverse fracture sets are consistent with the main Pyrenean shortening direction $\sim N10$ (e.g. Teixell, 1996; Beaudoin *et al.*, 2015). Note that the mean orientation measured in the Roncal valley ($\sim N0$ – $N10$) slightly differs from that measured further east ($\sim N30^\circ$). This difference could relate to a $\sim 20^\circ$ clockwise rotation between the both areas, as a result of higher total shortening to the east (Larrasoana *et al.*, 2003; Oliva-Urcia & Pueyo, 2007; Pueyo Anchueta *et al.*, 2012; Urcia *et al.*, 2012). Abutting relationships (Fig. 4) suggest that longitudinal fractures post-dated transverse fractures. These longitudinal fractures are likely syn-thrusting in age. As attested by the presence of crystal fibre lineations, the development of bedding-parallel fractures was associated with intra or interbed shear, likely as a result

of folding, and thus during thrusting (e.g. Tavani *et al.*, 2015) (Fig. 4h). However, we cannot discard the possibility that they formed during fluid overpressure prior to macroscopic folding (Jessell *et al.*, 1994; Fowler, 1996; e.g. Evans & Fischer, 2012; Tavani *et al.*, 2015).

The occurrence of multiple sets of fractures, both transverse and longitudinal (e.g. Fig. 4) in about half of the sites, suggests the possibility of different tectonic phases, and hence, different timing of fracturing. It was not the purpose of our work to investigate thoroughly the relationship between fracture sets, and from our dataset, it is not possible to better constrain the different tectonic phases.

Conditions and timing of vein precipitation

Evidence of high fluid-rock interaction

Isotope analysis of $\delta^{18}O$ and $\delta^{13}C$ reveals that most veins and host rocks present a remarkable homogeneous isotopic composition (Fig. 9a–d). The minimum $\delta^{18}O$ of parent water ($\delta^{18}O_{\text{water}}$) range from +9 to +17‰ (SMOW), as calculated from $\delta^{18}O$ values of calcite veins and homogenization temperatures of primary aqueous fluid inclusions, using the fractionation factor of Friedman & O'Neil (1977) (Fig. 9f). This range of values is similar to those observed in veins and host sediments close to the Monte Perdido thrust, and of adjacent eastern basins of the Pyrenean foreland (Travé *et al.*, 1997, 1998; Lacroix *et al.*, 2011, 2014). These values are consistent with water partially re-equilibrated with surrounding sedimentary rocks during burial (Longstaffe, 1987; Sharp, 2009). This indicates high water-rock interaction, resulting in the partial buffering of water isotopic composition by the carbonate fraction of the host-rock, before vein calcite precipitation (Bradbury & Woodwell, 1987). Any fluid flow was not acting long enough or in a sufficient volume to promote isotopic disequilibrium with the rocks (Bradbury & Woodwell, 1987; Kirschner & Kennedy, 2001). Few exceptions exist. For example, in the south-western part of Roncal valley, isotopic disequilibrium between vein calcites and their host-rock argue for rather low water-rock interaction (Fig. 9f). Calculated $\delta^{18}O_{\text{water}}$ (0–5‰) are compatible with Paleogene marine waters ($\delta^{18}O_{\text{water}}$ (SMOW) = -0.3 – -1.2 ‰) (Lear *et al.*, 2000) that have been only slightly buffered by host-rock carbonates (Sheppard, 1986; Longstaffe, 1987). However, the low salinities (<0.2 wt% eq. NaCl) recorded by primary fluid inclusions (Fig. 12) suggest the inflow of meteoric-derived water, likely through syn- and post-folding large scale fractures affecting the Paleocene-lower Ypresian carbonates.

Evidence of two stages of vein formation

The analysis of 254 fluid inclusions provide a range of T_h from 130 °C to nearly 300 °C through the entire studied

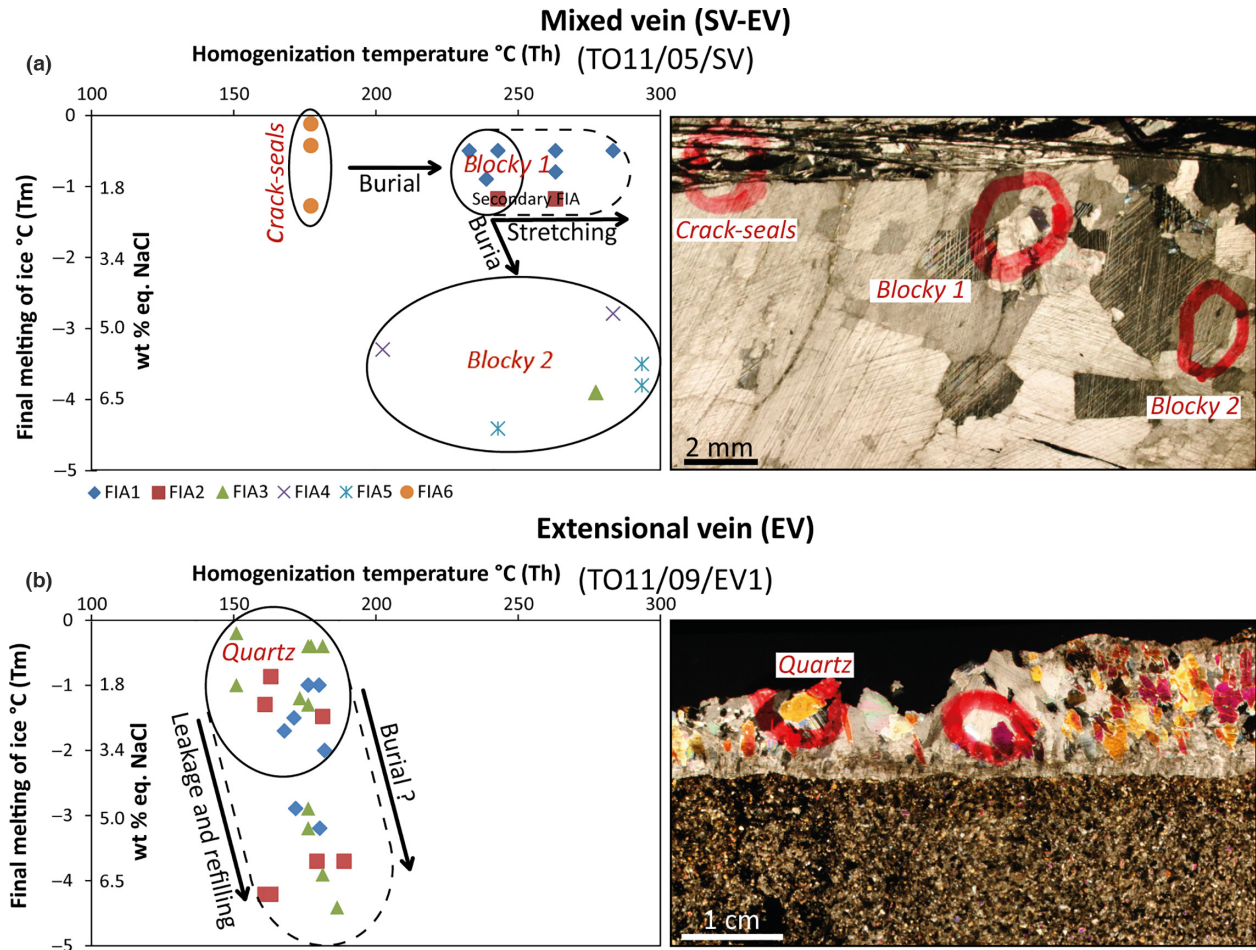


Fig. 13. Left: Th versus Tm crossplots of two samples from the Torla valley, represented by Fluid Inclusion Assemblages (FIA), with evidence of stretching (a) and of leakage and refilling (b). Right: microphotographs showing the location of measured fluid inclusions. Crack-seals correspond to the sheared border of the SV-EV vein, blocky 1 and blocky 2 to the centre of the vein (blocky zone). FIA: Fluid Inclusion Assemblage.

area (Fig. 11). Highest Th (>200 °C) are consistent with those reported by Lacroix *et al.* (2011) (Th = 120–250 °C), who focused their analysis on two thrusts of the Torla valley (Fig. 14a). However, this contrasts with the range of Th values of primary fluid inclusions (70–180 °C) reported by Izquierdo-Llavall *et al.* (2013), who studied 15 veins mostly located in longitudinal fractures of the Eocene turbidites. They focused their analysis on extensional veins and en-echelon veins formed during the development of cleavage and folding. The low Th when compared to temperatures of cleavage development (140–215 °C) (Izquierdo-Llavall *et al.*, 2013) suggests that fractures were filled during exhumation of the fold and thrust belt, in a retrograde behaviour.

A key observation of our petrographical and microthermometric analysis is the evidence of two stages of vein formation in the Sierras Interiores (labelled E1 and E2), with increasing temperature and salinity. This observation is based on (i) the presence of SV-EV veins showing

two distinct mineralogical textures (crack-seal on the border and blocky calcite in the centre) that we interpret as the mode-I reactivation of pre-existent shear veins (Figs 7, 8 and 13), and (ii) in the same veins, the observation of higher Th and salinities in the central blocky zones (Th generally above 190 °C and salinity up to twice that of seawater) compared to the crack-seal zones (Th generally below 220 °C and salinity below seawater) (Fig. 11). This interpretation is also supported by the large range of Th and salinities (126–280 °C and 0–7.7 wt% NaCl, respectively) of extensional veins, covering the values of both the border and the centre of SV-EV veins. In extensional veins, lowest temperature and salinity values of primary fluid inclusions are similar to those recorded in the border of shear veins, suggesting similar conditions of formation (stage E1). Some primary inclusions were then partially overheated, leaked and refilled at temperature and salinity conditions similar to those prevailing during precipitation of blocky calcite

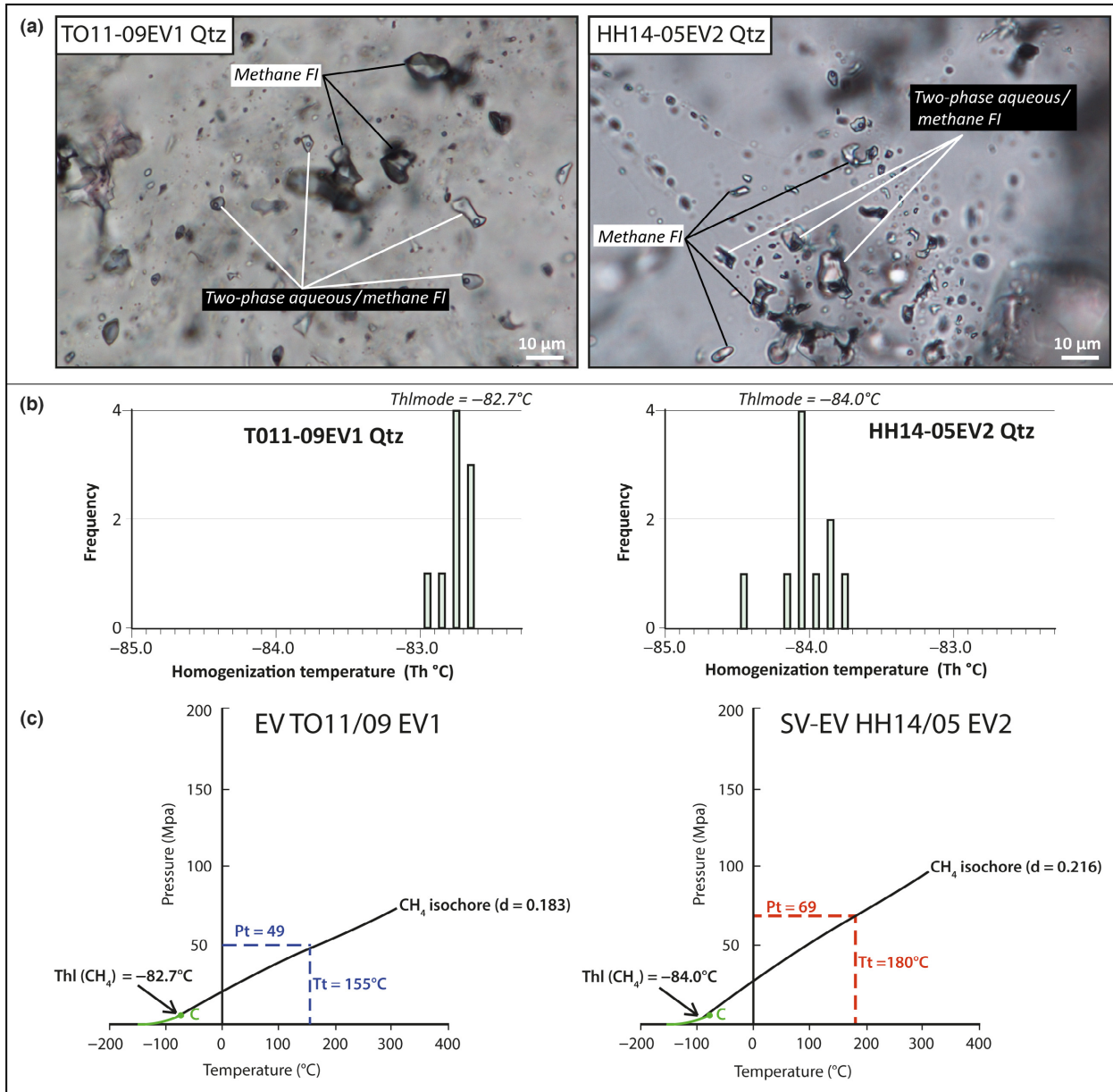


Fig. 14. (a) Photographs of two phase aqueous / methane, and methane fluid inclusions, belonging to the same FIA. The various gas/liquid ratios of two-phase inclusions (HH14-05EV2 Qtz) suggest heterogeneous entrapment. (b) Frequency plots of measured homogenization temperatures of methane fluid inclusions (Thl). The mode (Thl_{mode}) is also indicated. (c) P-T diagrams for methane inclusions. The isochore was calculated from their Thl_{mode} and from the minimum Th (=Tt) of two-phase aqueous/methane fluid inclusions. See text for details.

in SV-EV veins and in other extensional veins (stage E2) (Fig. 13). Finally, high Th and salinities measured in secondary fluid inclusions of extensional veins are close to those of primary fluid inclusions of the blocky zone of SV-EV veins (centre) (Fig. 11). These observations support a prograde behaviour between precipitation stages E1 and E2. These stages are recorded all along the turbiditic basin (Torla, Aragon and Hecho valleys). They are also noticed in the Monte-Perdido

thrust (Torla valley) by Lacroix *et al.* (2011) (Figs 2 and 11).

Evidence of brine circulation

Primary fluid inclusions in veins of stage E1 have salinities mostly lower than seawater (Fig. 15a). Low salinities can be explained either by the inflow of meteoric waters (e.g. Douglas *et al.*, 2003; Evans & Hobbs, 2003; Ramsey

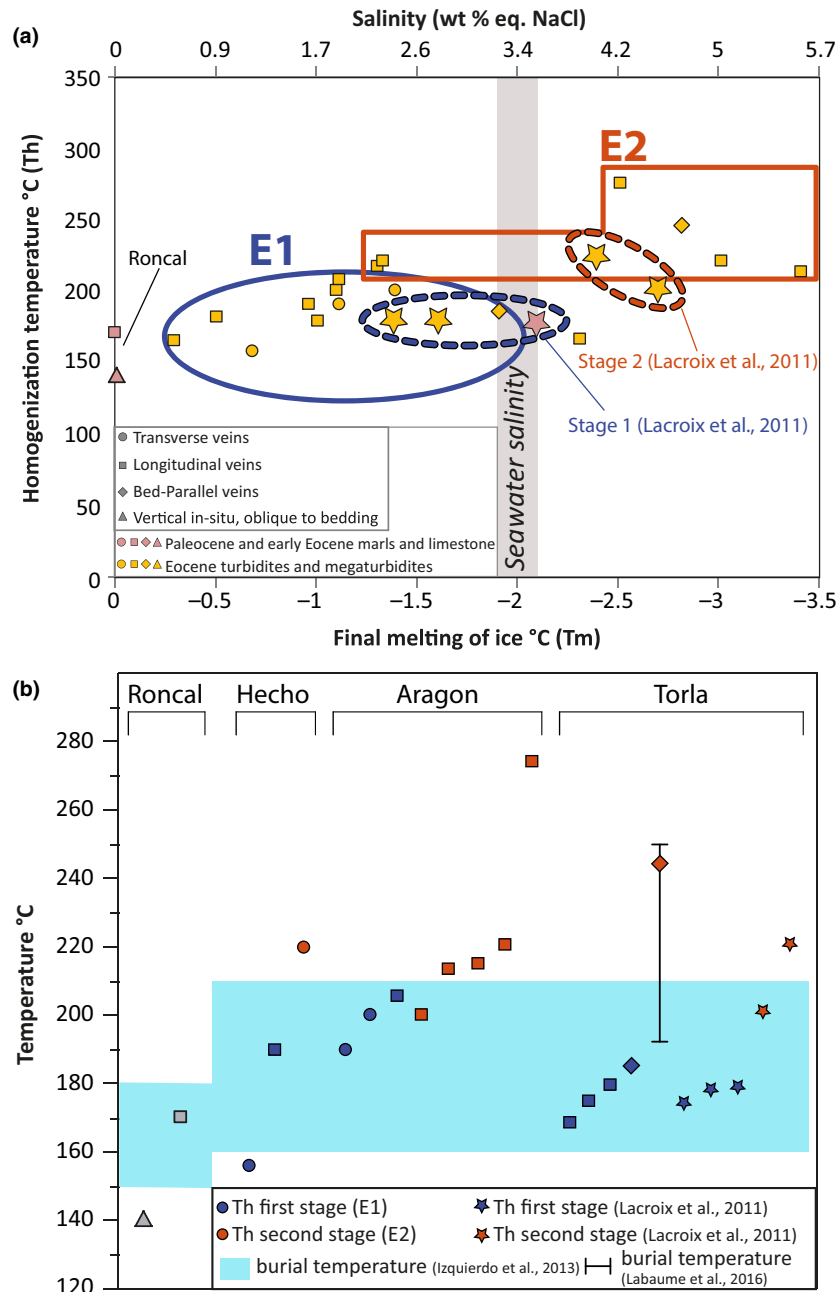


Fig. 15. (a) Th versus Tm diagram (modes) of primary and secondary fluid inclusions. The greyed zone corresponds to seawater salinity. (b) Homogenization temperatures (modes) compared to maximum burial temperatures calculated from vitrinite reflectance values of Izquierdo-Llavall *et al.* (2013) (light blue), and of Labaume *et al.* (2016) north of the Torla valley (black whisker).

& Chester, 2004; Bussolotto *et al.*, 2007; Beaudoin *et al.*, 2011) or by mineral dehydration, in particular the smectite to illite transition (Fitts & Brown, 1999; Brown *et al.*, 2001; Kim *et al.*, 2013). In the absence of isotopic analyses of fluid inclusions (e.g. H and O), we cannot discriminate between these two hypotheses (e.g. Fitz-Diaz *et al.*, 2011). However, Bauluz *et al.* (2012) and Izquierdo-Llavall *et al.* (2013) have shown that smectite illitization has been particularly efficient in turbidites of the Jaca basin,

at temperatures up to *ca.* 200 °C. Th of primary fluid inclusions measured in the border of shear veins (155–205 °C) are compatible with this latter mechanism.

Aqueous inclusions trapped in blocky calcite during the stage E2 have salinity frequently above seawater (Fig. 15a). Since Cl is a conservative element, high Cl concentrations in subsurface waters mainly result from subaerial evaporation, or subsurface dissolution of evaporites (Warren, 2006). Veins with important salinities

have been found in Paleocene carbonates and Eocene turbidites, which were deposited in open marine environments (Labaume *et al.*, 1985; Teixell, 1996; Huyghe *et al.*, 2009). Therefore, vein-filling minerals precipitated from water having acquired its higher salinity elsewhere (Fig. 15a). The only evaporitic deposits known in the area are those of Upper Triassic age (Teixell, 1996; Labaume *et al.*, 2016). Because highest salinities are found close to major thrusts (Larra and Monte Perdido) (Fig. 12), thrust faults may have acted as fluid conduits for brines having interacted with Triassic evaporites (e.g. Fyfe & Kerrich, 1985; Travé *et al.*, 2000; Roure *et al.*, 2005). A similar mechanism has already been documented in the Gavarnie thrust, few kilometres north of the study zone (McCaig *et al.*, 2000), and in the east of the Jaca basin (Mansurbeg *et al.*, 2009). The latter authors found evidence for the migration of brines with very high salinities (up to 18 wt% eq. NaCl.), trapped in calcite cement of the Hecho turbidites. Our results suggest that such brines also migrated in fractures in the northern part of the basin (Fig. 12).

Another evidence for the likely external origin of these brines lies in their high Th up to *ca.* 300 °C (Fig. 15b). In the turbiditic though, the burial temperatures provided by several studies barely exceeded *ca.* 220 °C (Izquierdo-Llavall *et al.*, 2013; Labaume *et al.*, 2016). We propose therefore that brines locally were in thermal disequilibrium with enclosing rock. The inflow of hot waters from deeper levels may have taken place during fracturing and re-opening of preexistent veins (e.g. Evans & Battles, 1999; Evans & Hobbs, 2003; Beaudoin *et al.*, 2011; Evans & Fischer, 2012). To maintain local thermal disequilibrium with the host-rock, water flow occurred as pulses of short time duration (<100 ka) through fractures (Bons *et al.*, 2014).

P-T conditions and timing of fluid circulation

Based on petrographical observations, heterogeneous entrapment of CH₄ and H₂O observed in two veins is interpreted to have taken place during stage E1 (sample TO11/09 EV1, longitudinal mineralized fracture, hosted in lower Lutetian turbidites) and stage E2 (sample HH14/05 EV2, transversal mineralized fracture, hosted in lower Lutetian turbidites) (Fig. 14a). These samples can be used to calculate the temperature and the fluid pressure at the time of entrapment (Goldstein, 2001). Within an FIA, a consistent pattern of Th in methane-saturated aqueous fluid inclusions should reflect the true entrapment temperature, allowing to calculate the pressure of entrapment using the isochore of methane inclusions (Goldstein, 2001). In the absence of such pattern, the lowest Th of aqueous fluid inclusions should be close to the temperature of entrapment, provided they were trapped from a single homogeneous aqueous fluid

(Goldstein, 2001). For the extensional longitudinal vein attributed to stage E1, a minimum Th of 155 °C for aqueous FIs, and a Th of -82.7 °C for methane inclusions give a pressure of 49 MPa when using the model of Bakker (1999). For the central part of the transversal shear vein (stage E2), we calculate a pressure of 69 MPa for a minimum Th of 180 °C (Fig. 14c). In lithostatic conditions, the calculated geothermal gradient exceeds 73 °C km⁻¹ and 62 °C km⁻¹ for stages E1 and E2 respectively, implying unrealistically low burial of 2–3 km. In hydrostatic conditions, the calculated geothermal gradient is 30 °C km⁻¹ for stage E1 and 25 °C km⁻¹ for stage E2, in line with geothermal gradients of foreland basins (22–24 °C km⁻¹) (Allen & Allen, 2013) and with the value of Lacroix *et al.* (2011) (34 °C km⁻¹). Accordingly, assuming more realistic hydrostatic conditions and using a Paleogene surface temperature of 10–15 °C (Zachos *et al.*, 1994), we calculate a minimum burial depth of *ca.* 5 km and *ca.* 7 km for stages E1 and E2 respectively. However, since fluid overpressure generation is a common mechanism in foreland basins (e.g. Beaudoin *et al.*, 2014b), these geothermal gradient should be used with caution.

We attempt in the following to date when Hecho turbidites reached depth of *ca.* 5 km and *ca.* 7 km using tectono-sedimentary reconstructions from the northern turbiditic basin and the Sierras Interiores (Carbayo *et al.*, 1972; De Rojas & Latorre, 1972; Del Valle *et al.*, 1972; Labaume *et al.*, 1985; Ríos Aragüés *et al.*, 1987, 1987b; e.g. Teixell *et al.*, 1989b; Teixell, 1990; Millán Garrido *et al.*, 1994; Teixell, 1996; Labaume *et al.*, 2016). The *ca.* 5 km sedimentary burial which might correspond to stage E1 was reached during the early Bartonian, at the end of the emplacement the Eaux-chaudes thrust unit. The *ca.* 7 km burial depth of for vein reactivation (stage E2) better corresponds to Priabonian to Rupelian times. Therefore, reactivation would have been synchronous with deposition of Campodarbe conglomerates and with intense fold propagation in the turbiditic basin due to the activation of the underlying Gavarnie thrust unit (Labaume *et al.*, 1985, 2016; Millán Garrido *et al.*, 1994; Teixell, 1996; Jolivet *et al.*, 2007; Teixell *et al.*, 2016). These results are in line with the study of Lacroix *et al.* (2011), who defined three stages of vein opening in thrust faults of the Monte-Perdido unit (Sierras Interiores). According to their study, the first stage of vein opening occurred at *ca.* 210 °C and 57 MPa from water with low salinity. Despite slightly higher P-T conditions, they also attributed this first stage to Eaux-Chaudes (Monte Perdido) thrusting. Similarly, they attributed the second stage (*ca.* 240 °C, *ca.* 65 MPa, salinity up to 5.9 wt% eq) to the emplacement of the underlying Gavarnie unit. Our results extend the links between fracture development, fluid flow and Eaux-Chaudes/Gavarnie thrusting to the entire northern part of the Jaca basin. The third stage of Lacroix *et al.* (2011) (<170 °C), attributed to late

exhumation, was not recorded in our samples except possibly in low temperature veins of the Hecho and Broto valleys ($T < 140$ °C).

Relative timing of fracturing and vein filling

In foreland basins, precipitation of calcite and quartz in fractures can take place both during fracturing and during reactivation of pre-existent fractures (Tavani *et al.*, 2015). In the Jaca basin, E1 veins are found in transverse fractures and longitudinal fractures. Therefore, we suggest that precipitation stage E1 took place likely during folding, at the end of, or after layer-parallel shortening. E2 veins are also found in transverse and longitudinal fractures. We suggest that they resulted from the tensile reactivation of joints or veins at higher P-T conditions, during active thrusting.

Synthesis fluid flow and fracturing in the Jaca basin

Hereafter, we propose a conceptual model linking the tectonic evolution to global fracturing pattern and paleohydrology of the northern Jaca basin (Fig. 16).

During the Ypresian, the morphology and sedimentary architecture of the basin was largely controlled by the emplacement of the Eaux-chaudes thrust unit in the Axial Zone (e.g. Labaume *et al.*, 1985, 2016; Teixell, 1996; Teixell *et al.*, 2016) (Fig. 16). In response to the southward migration of the deformational front (Labaume *et al.*, 2016), we propose that LPS-related transverse joints affected Maastrichtian to Ypresian sediments along the Sierras Interiores and the lower turbiditic basin.

From the Lutetian to the Bartonian, during the deposition of *ca.* 3 km Hecho turbidites in the foredeep (Labaume *et al.*, 1985, 2016; Mutti *et al.*, 1988; Millán Garrido *et al.*, 2006), we propose that longitudinal fractures developed together with the reactivation of former transverse joints, during incipient folding. In the lower turbidites, the transformation of smectite into illite could have favoured the release of low salinity waters in the porewaters (Bauluz *et al.*, 2012). Reactivated and newly formed LPS and syn-folding joints were then filled with calcite or calcite – quartz precipitates, corresponding to the first stage of vein precipitation (E1), at $T < 200$ °C (Fig. 15).

During the Priabonian and the early Rupelian, the turbiditic basin was refolded by Gavarnie thrusting (Labaume *et al.*, 1985) (Fig. 16). In the Axial Zone, warm, saline metamorphic waters were expelled along the Gavarnie thrust (McCaig *et al.*, 2000). In the Sierras Interiores and lower turbiditic basin, we propose the re-opening of previous veins (LPS and syn-folding fracture filling), resulting in stage E2 veins. These veins locally

recorded the circulation of saline water in thermal disequilibrium with the host-rock. In the upper turbidites and in Paleocene carbonates of the Roncal area, cover thrusting and fracture development possibly favoured the local circulation of meteoric water. Coevally, meteoric water flows along the Jaca thrust (Lacroix *et al.*, 2014), and folding-related fractures of the Pico del Aguila anticline (Sierras Exteriores) allowed small-scale, interformational, vertical fluid migration between reservoirs (Beaudoin *et al.*, 2015). Priabonian and early Rupelian times were thus associated to a more open palaeohydrological behaviour, likely due to thrusting and joint/vein opening.

The emplacement of successive thrusts during the Priabonian – Rupelian was thus the main driver of the paleohydrology of the Jaca basin, and resulted in a partition between its northern part (predominance of formation and metamorphic hydrothermal waters) and its southern part (inflow of meteoric waters).

Implications

Due to their impact on the evolution of reservoirs, the links between fracture development and fluid circulation in foreland fold and thrust belts has been the subject of active research in the last decades (Evans & Battles, 1999; Ramsey & Onasch, 1999; Ferket *et al.*, 2000, 2002; Kirkwood *et al.*, 2000; Machel *et al.*, 2000; Douglas *et al.*, 2003; Evans & Hobbs, 2003; Bellahsen *et al.*, 2006; Katz *et al.*, 2006; Wall *et al.*, 2006; Breesch *et al.*, 2009; Fischer *et al.*, 2009; Amrouch *et al.*, 2010a,b, 2011; Callot *et al.*, 2010; Beaudoin *et al.*, 2011, 2014b; Barbier *et al.*, 2012a,b; Evans & Fischer, 2012; Evans *et al.*, 2012). In the south Pyrenean fold and thrust belt, where the impact of thrust emplacement on fluid flow has been extensively studied (e.g. Rye & Bradbury, 1988; Travé *et al.*, 1997, 1998, 2007; McCaig *et al.*, 2000; Lacroix *et al.*, 2011, 2014; Beaudoin *et al.*, 2015; Cruset *et al.*, 2016), the similarity between the geochemical and microthermometric characteristics of veins found in the Axial zone, the Jaca, Ainsa and Catalan basins suggests common mechanisms of fluid flow and vein formation. Most of the above-mentioned studies highlighted the presence of hydrothermal waters or brines in thrust faults, and the mixing between waters of distinct origins, in accordance with our proper results.

Travé *et al.* (1997, 1998) have shown that in the north of the Ainsa basin, the early emplacement of the Cotiella Nappe (Ypresian – Lutetian) was associated with mixing of formation water and upward-ascending brines. At the same time, we propose the stage E1 in the Jaca basin. During the Bartonian and the Priabonian, as tectonic shortening had progressed westward, the upward flow of warm hypersaline waters ($T > 200$ °C), and their mixing with meteoric or formation water, occurred along the

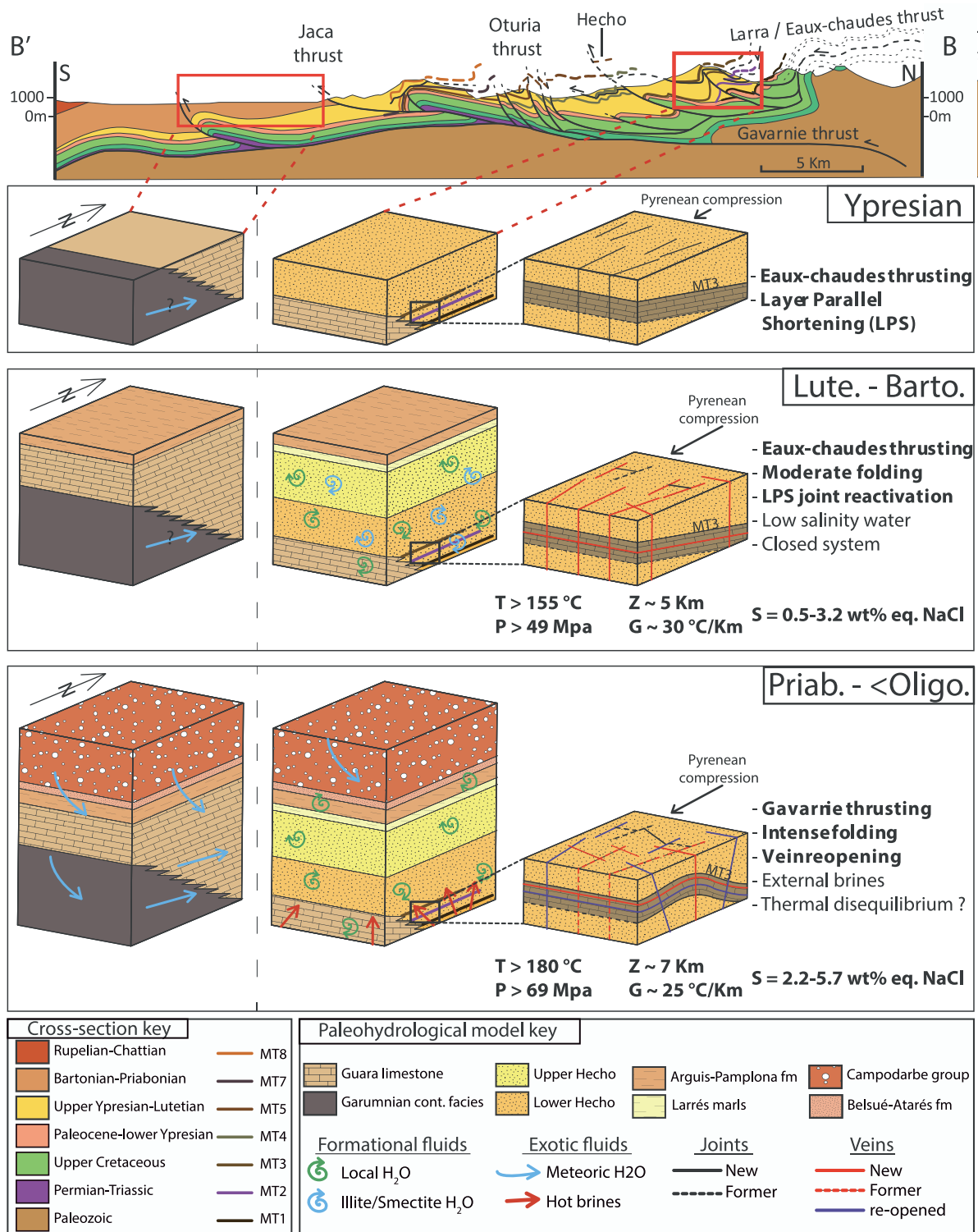


Fig. 16. Conceptual model of the evolution of fracturing and fluid circulation in the southern part of the turbiditic basin and the Sierras Interiores from the Ypresian to the Rupelian (see text for details). The cross-section is redrawn from Labaume *et al.* (1985) (location on Fig. 2 (BB')). *T* = temperature; *P* = pressure; *Z* = sedimentary burial; *G* = geothermal gradient; *S* = salinity.

Gavarnie thrust unit, north of the Jaca basin (Rye & Bradbury, 1988; McCaig *et al.*, 2000). As shown in the present study, the inflow of these exotic waters was likely

recorded southward, in the Sierras Interiores and lower turbiditic basin, coeval to intense fracturing and folding. These observations suggest that the westward

propagation of the orogenic wedge was associated with an evolution of fluid signatures, passing from formation waters to the ingress of brines having interacted with Triassic rocks at depth. Such fluid flow was favoured by southward thrust propagation and wide scale fracture development or reactivation. The role of LPS-related fractures and thrusts on fluid migration has also been demonstrated in more external domains of the south Pyrenean fold and thrust belt, where meteoric water is more clearly involved. In the Jaca basin, meteoric water migrated downward along the Jaca thrust (Lacroix *et al.*, 2014) and small-scale interformational fluid migration was favoured by fold-related fracturing in the Sierras Exteriores (Beaudoin *et al.*, 2015). In the eastern Catalan basin, thrust planes and LPS-related joints also favoured fluid circulation during middle Eocene to Oligocene shortening. Such fluids were of meteoric parentage close to the Escala thrust and in the El Guix anticline (Travé *et al.*, 2007), but possibly basement-derived and hydrothermal in the Puig-Reig anticline (Cruset *et al.*, 2016).

This evolution from a closed and stratified, to a more open hydrological system during thrust propagation and associated fracturing has been also described in other fold and thrust belts (Evans & Battles, 1999; Swennen *et al.*, 2000; Van Geet *et al.*, 2002; Evans & Hobbs, 2003; Schneider, 2003; Wall *et al.*, 2006; Vilasi *et al.*, 2009; Evans, 2010; Evans *et al.*, 2012). For example, in the Appalachian province, fluid flow was mainly restricted to permeable layers bounded by low-permeability marls and shales, but hydrothermal waters of metamorphic or connate parentage also migrated along active decollement levels and fracture networks (Evans & Battles, 1999; Evans & Hobbs, 2003; Evans, 2010; Evans *et al.*, 2012). A very close paleohydrological behaviour was described in the Albanides, which recorded the transition from a closed system to the active migration of hydrothermal water having interacted with underlying evaporites (Swennen *et al.*, 2000; Van Geet *et al.*, 2002; Wall *et al.*, 2006; Vilasi *et al.*, 2009), and in the Venezuelan foreland basin system, where large-scale thrusting favoured connection between several productive reservoirs (Schneider, 2003). However, contrary to the South Pyrenean Foreland Basin, these fold and thrust belts exhibit the wide scale remobilization of deeply infiltrated warm meteoric water toward the entire foreland basin, which had a crucial impact on their thermal and diagenetic evolution. Examples of the prominent role of meteoric water have been provided for the Canadian and American Rockies (Bighorn basin, Wyoming, USA) (Douglas *et al.*, 2003; Katz *et al.*, 2006; Beaudoin *et al.*, 2011, 2014b; Barbier *et al.*, 2012b), the Appalachian province (Evans & Battles, 1999; Ramsey & Onasch, 1999; Kirkwood *et al.*, 2000; Evans & Hobbs, 2003; Evans, 2010), the Bolivian sub Andean zone (SAZ) (Husson & Moretti, 2002), the

Veracruz basin (Sierras Madre, Mexico) (Ferket *et al.*, 2000, 2002), the Albanides (Vilasi *et al.*, 2009) or the northern Emirates (Callot *et al.*, 2010).

Finally, the South Pyrenean fold and thrust belt represents a striking example of the impact of large-scale thrust tectonics on mesoscale fracture development and reactivation, and associated large-scale fluid flow. Although its global paleohydrological evolution compares well to other fold and thrust belts, lateral propagation of shortening resulted in the coeval presence of distinct fluid flow regimes along strike, controlled by the structural evolution of the orogenic belt. These results emphasize the necessity to consider spatiotemporal fracture evolution in fluid-flow modelling of fold and thrust belts. Our study also points to how fluid analysis can help to discuss the large scale evolution of fracture development in foreland basins.

CONCLUSIONS

- The analysis of stable isotopes and fluid inclusions of syn-tectonic veins, coupled to that of the fracture network, has been used to reconstruct the fluid circulation pattern of the Jaca Basin, as part of the South Pyrenean fold and thrust belt, during the Paleogene.
- The fracture network recognized along the Sierras Interiores and the turbiditic basin comprises two major sets of joints/veins: (i) a N-S set, transverse, and (ii) an E-W longitudinal set that we proposed to be related to layer parallel shortening (LPS) and folding respectively.
- Longitudinal and transverse calcite and calcite – quartz veins have similar petrographic, isotopic and fluid inclusion characteristics. They precipitated at high temperature ($T > 160$ °C) from highly buffered waters of variable salinity.
- In the Sierras Interiores and the northern turbiditic basin, two stages of vein precipitation are recognized. During the first stage, aqueous fluid inclusions trapped in extensional and shear veins record T_h of 155–205 °C, and salinities lower than seawater, likely as a result of fresh water expelled by the smectite-to-illite transformation. During the second stage, inclusions recorded higher temperature ($T_h = 215$ –270 °C) and salinity, suggesting the inflow of exotic brines having interacted with underlying Triassic evaporites. In the southern turbiditic basin, veins recorded the inflow of meteoric waters ($T < 170$ °C).
- We relate the two stages to thrust activity. The first stage recorded in the northern part of the basin might have taken place at *ca.* 5 km burial, during Eaux-chaudes thrusting (middle Lutetian to Bartonian). The second stage might have taken at *ca.* 7 km burial, coevally to Gavarnie thrusting (Priabonian – early Rupelian).

- In the Sierras Interiores and the lower turbiditic basin, we highlight the progressive transition from a rather closed, to a more open hydrological system along with thrust propagation, due to folding and fracturing.
- The South Pyrenean fold and thrust belt makes a good example of both lateral and longitudinal variations of the fluid flow regime at a given time, making a good analogue to fold and thrust belts showing a diachronous frontal and lateral thrust propagation.

ACKNOWLEDGEMENTS

The first author benefited from a PhD grant of the French Ministry for Higher Education and Research (MENESR). The authors would like to thank P. Labaume for useful discussions about the geodynamic evolution of the Jaca basin. J.P. Girard is thanked for valuable discussions on fluid inclusions and data presentation. We thank M. De Rafélis for his help and support during geochemical analyses. The manuscript greatly benefited from the reviews of N. Beaudoin and N. Bellahsen.

SUPPORTING INFORMATION

Additional Supporting Information may be found in the online version of this article:

Figure S1. Th versus Tm diagrams, showing means and standard deviations for each primary and secondary FIA, analysed in extensional (EV) and SV-EV veins (crack-seal and blocky zones). Salinity in wt % eq. NaCl.

Table S1. Detailed location of fracture sites. Analytical techniques used at each site are also reported (vitrinite reflectance from Izquierdo *et al.* (2013) and Labaume *et al.* (2016)). Report to Fig. 12 to localized microthermometric analyses (R1; R2; H1-H3; A1-A3 and B1-B6).

Table S2. Results of isotopic analyses. n: not determined.

REFERENCES

- AL-AASM, I.S., LONNÉE, J. & CLARKE, J. (2002) Multiple fluid flow events and the formation of saddle dolomite: case studies from the middle Devonian of the Western Canada sedimentary basin. *Mar. Pet. Geol.*, **19**, 209–217.
- ALLEN, P.A. & ALLEN, J.R. (2013) *Basin Analysis: Principles and Application to Petroleum Play Assessment*. John Wiley & Sons, Oxford.
- AMROUCH, K., LACOMBE, O., BELLAHSEN, N., DANIEL, J.M. & CALLOT, J.P. (2010a) Stress and strain patterns, kinematics and deformation mechanisms in a basement-cored anticline: sheep Mountain Anticline, Wyoming. *Tectonics*, **29**, TC1005. <https://doi.org/10.1029/2009TC002525>.
- AMROUCH, K., ROBION, P., CALLOT, J.-P., LACOMBE, O., DANIEL, J.-M., BELLAHSEN, N. & FAURE, J.-L. (2010b) Constraints on deformation mechanisms during folding provided by rock physical properties: a case study at sheep mountain anticline (Wyoming, USA). *Geophys. J. Int.*, **182**, 1105–1123.
- AMROUCH, K., BEAUDOIN, N., LACOMBE, O., BELLAHSEN, N. & DANIEL, J.M. (2011) Paleostress magnitudes in folded sedimentary rocks. *Geophys. Res. Lett.*, **38**, L17301. <https://doi.org/10.1029/2011GL048649>.
- BAKKER, R.J. (1999) Adaptation of the Bowers and Helgeson (1983) equation of state to the H₂O–CO₂–CH₄–N₂–NaCl system. *Chem. Geol.*, **154**, 225–236.
- BARBIER, M., HAMON, Y., CALLOT, J.-P., FLOQUET, M. & DANIEL, J.-M. (2012a) Sedimentary and diagenetic controls on the multiscale fracturing pattern of a carbonate reservoir: the Madison formation (Sheep Mountain, Wyoming, USA). *Mar. Pet. Geol.*, **29**, 50–67.
- BARBIER, M., LEPRÉTRE, R., CALLOT, J.-P., GASPARRINI, M., DANIEL, J.-M., HAMON, Y., LACOMBE, O. & FLOQUET, M. (2012b) Impact of fracture stratigraphy on the paleo-hydrogeology of the Madison limestone in two basement-involved folds in the Bighorn Basin, (Wyoming, USA). *Tectonophysics*, **576**, 116–132.
- BAULUZ, B., YUSTE, A., MAYAYO, M., RODRÍGUEZ-NAVARRO, A. & GONZÁLEZ-LÓPEZ, J. (2012) Microtexture and genesis of clay minerals from a turbiditic sequence in a Southern Pyrenees Foreland Basin (Jaca Basin, Eocene). *Clay Miner.*, **47**, 303–318.
- BEAUDOIN, N., BELLAHSEN, N., LACOMBE, O. & EMMANUEL, L. (2011) Fracture-controlled paleohydrogeology in a basement-cored, fault-related fold: sheep Mountain Anticline, Wyoming, United States. *Geochem. Geophys. Geosyst.*, **12**, Q06011.
- BEAUDOIN, N., BELLAHSEN, N., LACOMBE, O., EMMANUEL, L. & PIRONON, J. (2014a) Crustal-scale fluid flow during the tectonic evolution of the Bighorn Basin (Wyoming, USA). *Basin Res.*, **26**, 403–435.
- BEAUDOIN, N., LACOMBE, O., BELLAHSEN, N., AMROUCH, K. & DANIEL, J.-M. (2014b) Evolution of pore-fluid pressure during folding and basin contraction in overpressured reservoirs: insights from the Madison–Phosphoria carbonate formations in the Bighorn Basin (Wyoming, USA). *Mar. Pet. Geol.*, **55**, 214–229.
- BEAUDOIN, N., HUYGHE, D., BELLAHSEN, N., LACOMBE, O., EMMANUEL, L., MOUTHEREAU, F. & OUANHON, L. (2015) Fluid systems and fracture development during syn-depositional fold growth: an example from the Pico Del Aguila Anticline, sierras exteriores, Southern Pyrenees, Spain. *J. Struct. Geol.*, **70**, 23–38.
- BEAUMONT, C., MUÑOZ, J.A., HAMILTON, J. & FULLSACK, P. (2000) Factors controlling the Alpine evolution of the central Pyrenees inferred from a comparison of observations and geodynamical models. *J. Geophys. Res. Solid Earth*, **105**, 8121–8145.
- BELLAHSEN, N., FIORE, P. & POLLARD, D.D. (2006) the role of fractures in the structural interpretation of Sheep Mountain Anticline, Wyoming. *J. Struct. Geol.*, **28**, 850–867.
- BERGBAUER, S. & POLLARD, D.D. (2004) A new conceptual fold-fracture model including prefolding joints, based on the

- Emigrant Gap Anticline, Wyoming. *Geol. Soc. Am. Bull.*, **116**, 294–307.
- BODNAR, R. (1993) Revised equation and table for determining the freezing point depression of H₂O-NaCl solutions. *Geochim. Cosmochim. Acta*, **57**, 683–684.
- BONS, P.D., ELBURG, M.A. & GOMEZ-RIVAS, E. (2012) A review of the formation of tectonic veins and their microstructures. *J. Struct. Geol.*, **43**, 33–62.
- BONS, P.D., FUSSWINKEL, T., GOMEZ-RIVAS, E., MARKL, G., WAGNER, T. & WALTER, B. (2014) Fluid mixing from below in unconformity-related hydrothermal ore deposits. *Geology*, **42**, 1035–1038.
- BRADBURY, H.J. & WOODWELL, G.R. (1987) Ancient fluid flow within foreland terrains. *Geol. Soc. Spec. Publ.*, **34**, 87–102.
- BRANELLEC, M., CALLOT, J., NIVIÈRE, B. & RINGENBACH, J. (2015) The fracture network, a proxy for mesoscale deformation: constraints on layer parallel shortening history from the Malargüe Fold and Thrust Belt, Argentina. *Tectonics*, **34**, 623–647.
- BREESCH, L., SWENNEN, R. & VINCENT, B. (2009) Fluid flow reconstruction in hanging and footwall carbonates: compartmentalization by Cenozoic reverse faulting in the Northern Oman Mountains (UAE). *Mar. Pet. Geol.*, **26**, 113–128.
- BROWN, K.M., SAFFER, D.M. & BEKINS, B.A. (2001) Smectite diagenesis, pore-water freshening, and fluid flow at the toe of the nankai wedge. *Earth Planet. Sci. Lett.*, **194**, 97–109.
- BUSSOLOTTI, M., BENEDICTO, A., INVERNIZZI, C., MICARELLI, L., PLAGNES, V. & DELANA, G. (2007) Deformation features within an active normal fault zone in carbonate rocks: the gubbio fault (Central Apennines, Italy). *J. Struct. Geol.*, **29**, 2017–2037.
- CALLOT, J.-P., BREESCH, L., GUILHAUMOU, N., ROURE, F., SWENNEN, R. & VILASI, N. (2010) Paleo-fluids characterisation and fluid flow modelling along a regional transect in Northern United Arab Emirates (UAE). In: *Lithosphere Dynamics and Sedimentary Basins: The Arabian Plate and Analogues* (Ed. by K. Al Hosani, F. Roure, R. Ellison & S. Lokier), pp. 177–201.
- CANTARELLI, V., ALDEGA, L., CORRADO, S., INVERNIZZI, C. & CASAS-SAINZ, A. (2013) Thermal history of the Aragón-Béarn Basin (Late Paleozoic, Western Pyrenees, Spain); insights into basin tectonic evolution. *Italian J. Geosci.*, **132**, 443–462.
- CARBAYO, A., LEÓN, L. & PUIGDEFÀBREGAS, G. (1972) Mapa Geológico De España a Escala 1:50000. Hoja 117 (Ochagavía). *IGME, Spain*.
- CARDOZO, N. & ALLMENDINGER, R.W. (2013) Spherical projections with osxstereonet. *Comput. Geosci.*, **51**, 193–205.
- CHOUKROUNE, P. & GARRIDO, A. (1989) Les Pyrénées Vues Par Ecos: Une Image Inattendue!. *La Recherche*, **206**, 132–135.
- COOPER, M. (2007) Structural style and hydrocarbon prospectivity in fold and thrust belts: a global review. *Geol. Soc. Spec. Publ.*, **272**, 447–472.
- CRUSET, D., CANTARERO, I., TRAVÉ, A., VERGÉS, J. & JOHN, C.M. (2016) Crestal graben fluid evolution during growth of the Puig-Reig anticline (South Pyrenean Fold and Thrust Belt). *J. Geodyn.*, **101**, 30–50.
- DE ROJAS, B.J. & LATORRE, F. (1972) Mapa Geológico De España a Escala 1:50000. Hoja 175 (Sigüés). *IGME, Spain*.
- DEL VALLE, J., PUIGDEFÀBREGAS, C. & SÁNCHEZ, I. (1972) Mapa Geológico De España a Escala 1:50000. Hoja 143 (Navascués). *IGME, Spain*.
- DOUGLAS, T., CHAMBERLAIN, C., POAGE, M., ABRUZZESE, M., SHULTZ, S., HENNEBERRY, J. & LAYER, P. (2003) Fluid flow and the heart mountain fault: a stable isotopic, fluid inclusion, and geochronologic study. *Geofluids*, **3**, 13–32.
- ENGELDER, T. & PEACOCK, D.C. (2001) Joint development normal to regional compression during flexural-flow folding: the Lilstock Buttress Anticline, Somerset, England. *J. Struct. Geol.*, **23**, 259–277.
- EVANS, M.A. (2010) Temporal and spatial changes in deformation conditions during the formation of the central Appalachian fold-and-thrust belt: evidence from joints, vein mineral paragenesis, and fluid inclusions. *Geol. Soc. Am. Mem.*, **206**, 477–552.
- EVANS, M.A. & BATTLES, D.A. (1999) Fluid inclusion and stable isotope analyses of veins from the Central Appalachian valley and ridge province: implications for regional synorogenic hydrologic structure and fluid migration. *Geol. Soc. Am. Bull.*, **111**, 1841–1860.
- EVANS, M.A. & FISCHER, M.P. (2012) On the distribution of fluids in folds: a review of controlling factors and processes. *J. Struct. Geol.*, **44**, 2–24.
- EVANS, M.A. & HOBBS, G. (2003) Fate of ‘warm’ migrating fluids in the central Appalachians during the Late Paleozoic Alleghanian Orogeny. *J. Geochem. Explor.*, **78**, 327–331.
- EVANS, M.A., BEBOUT, G.E. & BROWN, C.H. (2012) Changing fluid conditions during folding: an example from the Central Appalachians. *Tectonophysics*, **576**, 99–115.
- FERKET, H., ROURE, F., SWENNEN, R. & ORTUNO, S. (2000) Fluid migration placed into the deformation history of fold-and-thrust belts: an example from the Veracruz Basin (Mexico). *J. Geochem. Explor.*, **69**, 275–279.
- FERKET, H., ORTUNO, S., ROURE, F. & SWENNEN, R. (2002) Diagenesis and fluid flow history in reservoir carbonates of the cordilleran foreland fold and thrust belt: the Cordoba platform (Eastern Mexico). *AAPG Search Dis. Art.*, #90011©2002 AAPG Hedberg Conference, May 14–18, 2002, Palermo – Mondello, Sicily, Italy.
- FISCHER, M.P., HIGUERA-DÍAZ, I.C., EVANS, M.A., PERRY, E.C. & LEFTICARIU, L. (2009) Fracture-controlled paleohydrology in a map-scale detachment fold: insights from the analysis of fluid inclusions in calcite and quartz veins. *J. Struct. Geol.*, **31**, 1490–1510.
- FITTS, T.G. & BROWN, K.M. (1999) Stress-induced smectite dehydration: ramifications for patterns of freshening and fluid expulsion in the N. Barbados Accretionary Wedge. *Earth Planet. Sci. Lett.*, **172**, 179–197.
- FITZ-DIAZ, E., HUDLESTON, P., SIEBENALLER, L., KIRSCHNER, D., CAMPRUBÍ, A., TOLSON, G. & PUIG, T.P. (2011) Insights into fluid flow and water-rock interaction during deformation of carbonate sequences in the Mexican Fold-Thrust Belt. *J. Struct. Geol.*, **33**, 1237–1253.
- FOWLER, T. (1996) Flexural-slip generated bedding-parallel veins from Central Victoria, Australia. *J. Struct. Geol.*, **18**, 1399–1415.
- FRIEDMAN, I. & O’NEIL, J.R. (1977) *Compilation of Stable Isotope Fractionation Factors of Geochemical Interest*. USGPO.
- FYFE, W. & KERRICH, R. (1985) Fluids and thrusting. *Chem. Geol.*, **49**, 353–362.
- GARRIDO, H.M., MORER, E.P., CARDONA, M.A., AGUADO, A.L., URCIÁ, B.O. & PEÑA, B.M. (2000) Actividad

- Tectónica Registrada En Los Depósitos Terciarios Del Frente Meridional Del Pirineo Central. *Rev. Soc. Geol. Esp.*, **13**, 279–300.
- GOLDSTEIN, R.H. (2001) Fluid Inclusions in sedimentary and diagenetic systems. *Lithos*, **55**, 159–193.
- GOLDSTEIN, R.H. & REYNOLDS, T.J. (1994) Systematics of fluid inclusions in diagenetic minerals: sepm short course. *Soc. Sediment. Geol.*, **31**, 199.
- HOAREAU, G., ODONNE, F., GARCIA, D., DEBROAS, E.-J., MONNIN, C., DUBOIS, M. & POTDEVIN, J.-L. (2015) Burial diagenesis of the Eocene Sobrarbe Delta (Ainsa Basin, Spain) inferred from dolomitic concretions. *J. Sediment. Res.*, **85**, 1037–1057.
- HUSSON, L. & MORETTI, I. (2002) Thermal regime of fold and thrust belts—an application to the Bolivian Sub Andean Zone. *Tectonophysics*, **345**, 253–280.
- HUYGHE, D., MOUTHEREAU, F., CASTELLTORT, S., FILLEAUDEAU, P.Y. & EMMANUEL, L. (2009) Paleogene propagation of the Southern Pyrenean thrust wedge revealed by finite strain analysis in frontal thrust sheets: implications for mountain building. *Earth Planet. Sci. Lett.*, **288**, 421–433.
- IZQUIERDO-LLAVALL, E., ALDEGA, L., CANTARELLI, V., CORRADO, S., GIL-PEÑA, I., INVERNIZZI, C. & CASAS, A.M. (2013) On the origin of cleavage in the central Pyrenees: structural and Paleo-thermal study. *Tectonophysics*, **608**, 303–318.
- JAMMES, S., MANATSCHAL, G., LAVIER, L. & MASINI, E. (2009) Tectonosedimentary evolution related to extreme crustal thinning ahead of a propagating ocean: example of the western Pyrenees. *Tectonics*, **28**, 4.
- JESSELL, M., WILLMAN, C. & GRAY, D. (1994) Bedding parallel veins and their relationship to folding. *J. Struct. Geol.*, **16**, 753–767.
- JOLIVET, M., LABAUME, P., MONIÉ, P., BRUNEL, M., ARNAUD, N. & CAMPANI, M. (2007) Thermochronology constraints for the propagation sequence of the south pyrenean basement thrust system (France–Spain). *Tectonics*, **26**, 5.
- KATZ, D.A., EBERLI, G.P., SWART, P.K. & SMITH, L.B. Jr (2006) Tectonic-hydrothermal brecciation associated with calcite precipitation and permeability destruction in Mississippian carbonate reservoirs, Montana and Wyoming. *AAPG Bull.*, **90**, 1803–1841.
- KIM, J.-H., TORRES, M.E., HONG, W.-L., CHOI, J., RIEDEL, M., BAHK, J.-J. & KIM, S.-H. (2013) Pore fluid chemistry from the second gas hydrate drilling expedition in the Ulleung Basin (Ubg2): source, mechanisms and consequences of fluid freshening in the central part of the Ulleung Basin, East Sea. *Mar. Pet. Geol.*, **47**, 99–112.
- KIRKWOOD, D., AYT-OUGUDAL, M., GAYOT, T., BEAUDOIN, G. & PIRONON, J. (2000) Paleofluid-Flow in a Foreland Basin, Northern Appalachians: from syntectonic flexural extension to taconian overthrusting. *J. Geochem. Explor.*, **69**, 269–273.
- KIRSCHNER, D.L. & KENNEDY, L.A. (2001) Limited syntectonic fluid flow in carbonate-hosted thrust faults of the front ranges, Canadian Rockies, inferred from stable isotope data and structures. *J. Geophys. Res. Solid Earth*, **106**, 8827–8840.
- LABAUME, P., SÉGURET, M. & SEYVE, C. (1985) Evolution of a turbiditic foreland basin and analogy with an accretionary prism: example of the Eocene South-Pyrenean Basin. *Tectonics*, **4**, 661–685.
- LABAUME, P., MERESSE, F., JOLIVET, M., TEIXELL, A. & LAHFID, A. (2016) Tectonothermal history of an exhumed thrust-sheet-top basin: an example from the South Pyrenean Thrust Belt. *Tectonics*, **35**, 1280–1313.
- LACROIX, B., BUATIER, M., LABAUME, P., TRAVÉ, A., DUBOIS, M., CHARPENTIER, D., VENTALON, S. & CONVERT-GAUBIER, D. (2011) Microtectonic and geochemical characterization of thrusting in a foreland basin: example of the South-Pyrenean Orogenic Wedge (Spain). *J. Struct. Geol.*, **33**, 1359–1377.
- LACROIX, B., CHARPENTIER, D., BUATIER, M., VENNEMANN, T., LABAUME, P., ADATTE, T., TRAVÉ, A. & DUBOIS, M. (2012) Formation of chlorite during thrust fault reactivation. Record of fluid origin and P–T Conditions in the Monte Perdido Thrust Fault (Southern Pyrenees). *Contrib. Miner. Petrol.*, **163**, 1083–1102.
- LACROIX, B., TRAVÉ, A., BUATIER, M., LABAUME, P., VENNEMANN, T. & DUBOIS, M. (2014) Syntectonic fluid-flow along thrust faults: example of the South-Pyrenean Fold-and-Thrust Belt. *Mar. Pet. Geol.*, **49**, 84–98.
- LAGABRIELLE, Y., LABAUME, P. & de SAINT BLANQUAT, M. (2010) Mantle Exhumation, crustal denudation, and gravity tectonics during cretaceous rifting in the pyrenean realm (Sw Europe): insights from the geological setting of the Iherzolite bodies. *Tectonics*, **29**, 4.
- LARRASOANA, J.C., PARÉS, J.M., MILLÁN, H., DEL VALLE, J. & PUEYO, E.L. (2003) Paleomagnetic, structural, and stratigraphic constraints on transverse fault kinematics during basin inversion: the Pamplona Fault (Pyrenees, North Spain). *Tectonics*, **22**, 1071.
- LEAR, C.H., ELDERFIELD, H. & WILSON, P. (2000) Cenozoic deep-sea temperatures and global ice volumes from Mg/Ca in Benthic Foraminiferal Calcite. *Science*, **287**, 269–272.
- LONGSTAFFE, F. (1987) Stable isotope studies of diagenetic processes. In: *Short Course in Stable Isotope Geochemistry of Low Temperature Fluids* (Ed. by T.K. Kyser), vol. 13, pp. 187–257. Mineralogical Association of Canada, Toronto.
- MACGREGOR, D.S. (1996) Factors controlling the destruction or preservation of giant light oilfields. *Petrol. Geosci.*, **2**, 197–217.
- MACHEL, H., CAVELL, P., BUSCHKUEHLE, B. & MICHAEL, K. (2000) Tectonically induced fluid flow in Devonian carbonate aquifers of the Western Canada sedimentary basin. *J. Geochem. Explor.*, **69**, 213–217.
- MANSURBEG, H., CAJA, M.A., MARFIL, R., MORAD, S., REMACHA, E., GARCIA, D., MARTIN-CRESPO, T., EL-GHALI, M.A.K. & NYSTUEN, J.P. (2009) Diagenetic evolution and porosity destruction of turbiditic hybrid arenites and siliciclastic sandstones of foreland basins: evidence from the Eocene Hecho Group, Pyrenees, Spain. *J. Sediment. Res.*, **79**, 711–735.
- MCCAIG, A.M., TRITTLA, J. & BANKS, D.A. (2000) Fluid mixing and recycling during pyrenean thrusting: evidence from fluid inclusion halogen ratios. *Geochim. Cosmochim. Acta*, **64**, 3395–3412.
- MILLÁN GARRIDO, H., AURELL, M. & MELÉNDEZ, A. (1994) Synchronous detachment folds and coeval sedimentation in the prepyrenean external Sierras (Spain): a case study for a tectonic origin of sequences and systems tracts. *Sedimentology*, **41**, 1001–1024.

- MILLÁN GARRIDO, H., JUAN, P. & SAINZ, C. (1995) El Frente Cabalgamiento Surpirenaico En El Extremo Occidental De Las Sierras Exteriores. *Rev. Soc. Geol. España*, **8**, 73–90.
- MILLÁN GARRIDO, H.A., URCIA, B.O. & JUAN, A.P. (2006) La Transversal De Gavarnie–Guara. Estructura Y Edad De Los Mantos De Gavarnie, Guara–Gèdre Y Guarga (Pirineo Centro–Occidental). *Geogaceta*, **40**, 35–38.
- MONTES, M.J. & BARNOLAS, A. (1992) Mapa Geológico De España a Escala 1:50000. Hoja 210 (Yebra De Basa). *IGME, Spain*.
- MOUTHÉREAU, F., FILLEAUDEAU, P.Y., VACHERAT, A., PIK, R., LACOMBE, O., FELLIN, M.G., CASTELLTORT, S., CHRISTOPHOUL, F. & MASINI, E. (2014) Placing limits to shortening evolution in the Pyrenees: role of margin architecture and implications for the Iberia/Europe Convergence. *Tectonics*, **33**, 2283–2314.
- MUÑOZ, J.A., BEAMUD, E., FERNÁNDEZ, O., ARBUÉS, P., DINARÈS-TURELL, J. & POBLET, J. (2013) The ainsa fold and thrust oblique zone of the Central Pyrenees: kinematics of a curved contractional system from paleomagnetic and structural data. *Tectonics*, **32**, 1142–1175.
- MUTTI, E., SÉGURET, M. & SGAVETTI, M. (1988) *Sedimentation and Deformation in the Tertiary Sequences of the Southern Pyrenees: Field Trip 7*. University of Parma, Parma.
- OLIVA-URCIA, B. & PUEYO, E.L. (2007) Rotational basement kinematics deduced from remagnetized cover rocks (Internal Sierras, Southwestern Pyrenees). *Tectonics*, **26**, <https://doi.org/10.1029/2006TC001955>.
- PASSCHIER, C.W. & TROUW, R.A.J. (2006) *Microtectonics*. 2nd edn, Springer-Verlag, Berlin, Germany. 366 pp.
- PUEYO ANCHUELA, Ó., PUEYO, E.L., POCOVÍ JUAN, A. & GIL IMAZ, A. (2012) Vertical axis rotations in fold and thrust belts: comparison of ams and paleomagnetic data in the western external sierras (Southern Pyrenees). *Tectonophysics*, **532–535**, 119–133.
- PUIGDEFÁBREGAS, C. (1975) La Sedimentación Molásica En La Cuenca De Jaca. *Inst. Estud. Piren.*, **104**, 1–188.
- QING, H. & MOUNTJOY, E. (1992) Large-scale fluid flow in the middle Devonian Presqu'île Barrier, Western Canada sedimentary basin. *Geology*, **20**, 903–906.
- RAMSEY, J.M. & CHESTER, F.M. (2004) Hybrid fracture and the transition from extension fracture to shear fracture. *Nature*, **428**, 63–66.
- RAMSEY, D.W. & ONASCH, C.M. (1999) Fluid migration in a cratonic setting: the fluid histories of two fault zones in the eastern midcontinent. *Tectonophysics*, **305**, 307–323.
- REMACHA, E. & FERNÁNDEZ, L.P. (2003) High-resolution correlation patterns in the turbidite systems of the Hecho Group (South-Central Pyrenees, Spain). *Mar. Pet. Geol.*, **20**, 711–726.
- RÍOS ARAGÜÉS, L.M., GALERA FERNÁNDEZ, J.M. & BARETTINO FRAILE, D. (1987) Mapa Geológico De España a Escala 1:50000. Hoja 146 (Bujaruelo). *IGME, Spain*.
- ROURE, F., CHOUKROUNE, P., BERASTEGUI, X., MUNOZ, J., VILLEN, A., MATHERON, P., BAREYT, M., SEGURET, M., CAMARA, P. & DERAMOND, J. (1989) Ecore deep seismic data and balanced cross sections: geometric constraints on the evolution of the Pyrenees. *Tectonics*, **8**, 41–50.
- ROURE, F., SWENNEN, R., SCHNEIDER, F., FAURE, J., FERKET, H., GUILHAUMOU, N., OSADETZ, K., ROBION, P. & VANDEGINSTE, V. (2005) Incidence and importance of tectonics and natural fluid migration on reservoir evolution in foreland fold-and-thrust belts. *Oil Gas Sci. Technol.*, **60**, 67–106.
- RYE, D.M. & BRADBURY, H.J. (1988) Fluid flow in the crust; an example from a Pyrenean thrust ramp. *Am. J. Sci.*, **288**, 197–235.
- SAURA, E. & TEIXELL, A. (2006) Inversion of small basins: effects on structural variations at the leading edge of the axial zone antiformal stack (Southern Pyrenees, Spain). *J. Struct. Geol.*, **28**, 1909–1920.
- SCHNEIDER, F. (2003) Basin modeling in complex area: examples from Eastern Venezuelan and Canadian Foothills. *Oil Gas Sci. Technol.*, **58**, 313–324.
- SHARP, Z. (2009) Application of stable isotope geochemistry to low-grade metamorphic rocks. In: *Low-Grade Metamorph.*, pp. 227–260. Blackwell Publishing Ltd., Oxford.
- SHEPPARD, S.M. (1986) Characterization and isotopic variations in natural waters. *Rev. Mineral. Geochem.*, **16**, 165–183.
- SPÖTL, C. & VENNEMANN, T.W. (2003) Continuous-flow isotope ratio mass spectrometric analysis of carbonate minerals. *Rapid Commun. Mass Spectrom.*, **17**, 1004–1006.
- STERNER, S.M. & BODNAR, R.J. (1984) Synthetic fluid inclusions in natural quartz I. Compositional types synthesized and applications to experimental geochemistry. *Geochim. Cosmochim. Acta*, **48**, 2659–2668.
- SWENNEN, R., MUSKHA, K. & ROURE, F. (2000) fluid circulation in the ionian fold and thrust belt (Albania): implications for hydrocarbon prospectivity. *J. Geochem. Explor.*, **69**, 629–634.
- TAVANI, S., STORTI, F., FERNÁNDEZ, O., MUÑOZ, J.A. & SALVINI, F. (2006) 3-D deformation pattern analysis and evolution of the Añiscló Anticline, Southern Pyrenees. *J. Struct. Geol.*, **28**, 695–712.
- TAVANI, S., STORTI, F., LACOMBE, O., CORRADETTI, A., MUÑOZ, J. & MAZZOLI, S. (2015) A review of deformation pattern templates in foreland basin systems and fold-and-thrust belts: implications for the state of stress in the frontal regions of thrust wedges. *Earth Sci. Rev.*, **141**, 82–104.
- TEIXELL, A. (1990) Mapa Geológico De España a Escala 1:50000. Hoja 176 (Jaca). *IGME, Spain*.
- TEIXELL, A. (1996) The Ansó Transect of the Southern Pyrenees: basement and cover thrust geometries. *J. Geol. Soc.*, **153**, 301–310.
- TEIXELL, A. (1998) Crustal structure and orogenic material budget in the West Central Pyrenees. *Tectonics*, **17**, 395–406.
- TEIXELL, A., GARCÍA SANSEGUNDO, J. & ZAMORANO, M. (1989b) Mapa Geológico De España a Escala 1:50000. Hoja 144 (Ansó). *IGME, Spain*.
- TEIXELL, A., MONTES, M.J., ARENAS, C. & GARRIDO, E.A. (1992) Mapa Geológico De España a Escala 1:50000. Hoja 208 (Uncastillo). *IGME, Spain*.
- TEIXELL, A., LABAUME, P. & LAGABRIELLE, Y. (2016) The crustal evolution of the West-Central Pyrenees revisited: inferences from a new kinematic scenario. *C.R. Geosci.*, **348**, <https://doi.org/10.1016/j.crte.015.10.010>.
- TRAVÉ, A., LABAUME, P., CALVET, F. & SOLER, A. (1997) Sediment dewatering and pore fluid migration along thrust faults in a foreland basin inferred from isotopic and elemental

- geochemical analyses (Eocene Southern Pyrenees, Spain). *Tectonophysics*, **282**, 375–398.
- TRAVÉ, A., LABAUME, P., CALVET, F., SOLER, A., TRITLLA, J., BUATIER, M., POTDEVIN, J.-L., SÉGURET, M., RAYNAUD, S. & BRIQUEU, L. (1998) Fluid migration during eocene thrust emplacement in the South Pyrenean foreland basin (Spain): an integrated structural, mineralogical and geochemical approach. *Geol. Soc. Spec. Publ.*, **134**, 163–188.
- TRAVÉ, A., CALVET, F., SANS, M., VERGÉS, J. & THIRLWALL, M. (2000) Fluid history related to the alpine compression at the margin of the South-Pyrenean foreland basin: the El Guix Anticline. *Tectonophysics*, **321**, 73–102.
- TRAVÉ, A., LABAUME, P. & VERGÉS, J. (2007) Fluid systems in foreland fold-and-thrust belts: an overview from the southern Pyrenees. In: *Thrust Belts and Foreland Basins*. Frontiers in Earth Sciences (Eds. by O. Lacombe, J. Lavé, F. Roure & J. Vergés), pp. 93–116. Springer.
- URCIA, B.O., CASAS, A., PUEYO, E. & JUAN, A.P. (2012) Structural and paleomagnetic evidence for non-rotational kinematics of the South Pyrenean frontal thrust at the western termination of the external Sierras (Southwestern Central Pyrenees). *Geol. Acta*, **10**, 125–144.
- VACHERAT, A., MOUTHEREAU, F., PIK, R., BERNET, M., GAUTHERON, C., MASINI, E., LE POURHET, L., TIBARI, B. & LAHFID, A. (2014) Thermal imprint of rift-related processes in orogens as recorded in the Pyrenees. *Earth Planet. Sci. Lett.*, **408**, 296–306.
- VAN GEET, M., SWENNEN, R., DURMISHI, C., ROURE, F. & MUCHEZ, P. (2002) Paragenesis of cretaceous to Eocene carbonates reservoirs in the Ionian fold and thrust belt (Albania): relation between tectonism and fluid flow. *Sedimentology*, **49**, 697–718.
- VERGÉS, J. & MUNOZ, J.A. (1990) Thrust sequence in the southern Central Pyrenees. *Bull. Soc. Géol. France*, **6**, 265–271.
- VERGÉS, J., MARZO, M. & MUÑOZ, J.A. (2002) Growth strata in foreland settings. *Sed. Geol.*, **146**, 1–9.
- VILASI, N., MALANDAIN, J., BARRIER, L., CALLOT, J.-P., AMROUCH, K., GUILHAUMOU, N., LACOMBE, O., MUSKA, K., ROURE, F. & SWENNEN, R. (2009) From outcrop and petrographic studies to basin-scale fluid flow modelling: the use of the Albanian natural laboratory for carbonate reservoir characterisation. *Tectonophysics*, **474**, 367–392.
- WALL, B.R.G., GIRBACEA, R., MESONJESI, A. & AYDIN, A. (2006) Evolution of fracture and fault-controlled fluid pathways in carbonates of the Albanides fold-thrust belt. *AAPG Bull.*, **90**, 1227–1249.
- WARREN, J.K. (2006) *Evaporites: Sediments, Resources and Hydrocarbons*. Springer Science & Business Media, Berlin.
- ZACHOS, J.C., STOTT, L.D. & LOHMANN, K.C. (1994) Evolution of early Cenozoic marine temperatures. *Paleoceanography*, **9**, 353–387.

Manuscript received 26 July 2016; In revised form 5 May 2017; Manuscript accepted 10 June 2017.